UNIVERSITY OF OKLAHOMA

GRADUATE COLLEGE

EXPERIMENTAL MODELING OF GEOMETRY AND EVOLUTION OF STRUCTURES ABOVE DUCTILE AND FRICTIONAL DETACHMENTS

A THESIS

SUBMITTED TO THE GRADUATE FACULTY

in partial fulfillment of the requirements for the

Degree of

MASTER OF SCIENCE

By

JIANJUN LI
Norman, Oklahoma
2016

EXPERIMENTAL MODELING OF GEOMETRY AND EVOLUTION OF STRUCTURES ABOVE DUCTILE AND FRICTIONAL DETACHMENTS

A THESIS APPROVED FOR THE
CONOCOPHILLIPS SCHOOL OF GEOLOGY AND GEOPHYSICS

BY

_____
Dr. Shankar Mitra, Chair

_____
Dr. Ze'ev Reches

_____
Dr. Matthew J. Pranter

ACKNOWLEDGEMENTS

I would like to express my sincere gratitude to Dr. Shankar Mitra for all his support and encouragement for the past 2 years of graduate study. Without his guidance and help, this thesis would not have been possible. I would also like to thank Dr. Ze'ev Reches and Dr. Matthew Pranter for the critical evaluation of the draft. Their suggestions were essential to the completion of this thesis. In Addition, I would like to thank Shiva Basnet, Ximeng Zu and Chance Morgan who have been great colleagues and partners. Their support and company have become an indispensable part in my graduate life. Last but not the least, I am grateful for all of what my parents have done for me. Their encouragement and sacrifice built what I have achieved so far.

TABLE OF CONTENTS

LIST OF TABLES

LIST OF FIGURES

ABSTRACT

Fold-thrust belts formed above ductile units like salt are typically characterized by detachment folds, whereas those formed above frictional detachments contain fault-related folds, such as fault-bend folds and duplexes. Analog models, using silica sand to represent sediments and silicone gel to represent salt, are conducted to study the fold geometry, fold-fault relations, and sequential development of structures formed in each setting and at the boundaries between the two settings. Variations in the orientations of the boundary between the frictional and ductile detachments, different thickness ratios between the ductile layer and overburden layers and the width of deformable backstop are investigated in this study. The results of experiments show different structure styles for the two settings: detachment folds with both forethrusts and backthrusts for ductile detachments, and duplex structures with only forethrusts for frictional detachments. A relatively steeper wedge was developed above a frictional detachment so that the deformation front above a ductile detachment propagated farther forward than the deformation front above a frictional detachment. Thrust faults connect across the two settings with significant changes in position and resulting changes in orientation. Backthrusts above ductile detachments typically terminate at the boundary. The experimental models are compared with surface and subsurface examples of salt basin boundaries. The results are applicable to the mapping of fold-thrust structures in areas of poor subsurface data quality.

CHAPTER 1: INTRODUCTION

1.1. *Introduction and Significance of the Problem*

The structural styles of fold-thrust belts are dependent on the mechanical stratigraphy. Frictional detachments are expected to result in early faulting within the structures and the formation of fault-related folds such as fault-bend and fault-propagation folds, and systems of these structures. Ductile detachments are expected to result in the formation of detachment folds, in which faulting usually occurs only after significant folding. Furthermore, the shape of the tapered Coulomb wedge defining the cross-sectional geometry of the entire belts varies between frictional ductile detachments, with the latter resulting in a narrower taper (Davis and Engelder, 1983). Therefore, transitions in the stratigraphy in the fold and thrust belt could result in changes in both the structural styles as well as the position of the thrust front, and the map-scale geometry.

Petroleum geologists are interested in mapping the geometry of prospect-scale structures formed above salt and frictional detachments. The quality of seismic data in fold-thrust belts is normally poor, thereby affecting the quality of the subsurface mapping. A better understanding of the controls of the mechanical stratigraphy on the structural styles will enable better prediction of both the structural geometry of individual structures, as well as the map-scale variations in regional structure, particularly along the boundary between areas with frictional and ductile substrates.

In this thesis, a series of sandbox models are developed as analog models of thin-skinned compressional structures above ductile and frictional detachments. Variations in structural styles resulting from variations in the orientations of the

boundary between the frictional and ductile detachments, different thickness ratios between the ductile layer and overburden layers and the width of deformable backstop are investigated.

The objectives of this study are to understand (1) the controls of ductile and frictional detachments on structural styles; (2) the location of thrust front and taper width for each style; (3) the controls of the shape of the detachment boundary on map trends; and (4) the propagation and connection of thrusts between regions with different mechanical stratigraphies.

1.2. *Background*

1.2.1. **Coulomb Wedge Model and Critical Taper Theory**

Chapple (1978) outlined the characteristics of thin-skinned fold-thrust belts to be a wedge-shaped deformation region tapering toward foreland. The basal detachment of the wedge dips towards the hinterland, whereas the surface slopes towards the foreland. A weak basal layer is commonly present and the deformation is driven by a horizontal compressional stress in the wedge. Based on these characteristics, Davis et al. (1983) and Dahlen et al. (1984) developed the Coulomb wedge model and critical taper theory to model the mechanics of thin-skinned fold-thrust belts and accretionary wedges as analogous to soil or snow being pushed by a bulldozer. The wedge deforms progressively from the hinterland to the foreland with the building up of a critical taper at each stage, followed the formation of a new frontal thrust.

Figure 1.1 (Dahlen and Suppe, 1988) represents a noncohesive, frictional Coulomb wedge, with a surface slope α and a basal dip β. σ_1 and σ_3 are the maximum

and minimum compressive stresses within the wedge. ψ_b is the angle between σ_1 and the base of the wedge. The angle between σ_1 and x-axis is denoted by ψ_0. θ_f is the dip angle of forethrusts with the base of the wedge and θ_b is the dip angle of backthrusts with the base of the wedge. ρ and ρ_w are the wedge density and water density. D is the local thickness of the water overburden along the direction of gravity.

The Coulomb wedge deforms until a critical taper is attained, after which it continues to grow at constant taper as additional material is encountered at the toe in front of a newly developed thrust fault (Davis et al., 1983). The theoretical critical taper of a noncohesive Coulomb wedge (Davis et al., 1983) is

$$\alpha + \beta = \frac{(1-\lambda)\mu_b + (1-\rho_w/\rho)\beta}{(1-\rho_w/\rho) + (1-\lambda)K}$$

where α is the topographic slope, β is the basal slope, λ is the ratio between pore fluid pressure and vertical normal traction exerted by the lithostatic overburden, μ_b is the basal coefficient of friction, ρ_w is the density of water, ρ is the density of the wedge material and K is a dimensionless quantity defined as

$$K \approx \frac{\sin\phi}{1-\sin\phi} + \frac{\sin^2\phi_b + \cos\phi_b\,(\sin^2\phi - \sin^2\phi_b)^{1/2}}{\cos^2\phi_b - \cos\phi_b\,(\sin^2\phi - \sin^2\phi_b)^{1/2}}$$

where ϕ is the angle of internal friction for the wedge material and ϕ_b is the angle of basal friction. The variation of K with μ and μ_b is shown in Figure 1.2. From the figure, it is concluded that an increase in basal friction decreases the K value which means an increase in the critical taper. An increase in internal friction has an opposite effect. Therefore, fold-thrust belts with a frictional detachment and a thin weak layer will have a larger taper angle than those with a thick and weak basal layer. This observation was confirmed by Davis and Engelder (1985, 1987), who looked specifically at fold

belts with a weak basal layer, such as salt. They proposed that if the basal detachment is in salt, which is extremely weak, the wedge is much more subtly tapered (1° or less) than in the absence of salt (8° ~ 12°) (Davis and Engelder, 1985, 1987). In other words, the deformation zone is wider at low basal friction than at high basal friction (Mulugeta, 1988; Mandal et al., 1997; Cotton and Koyi, 2000; Costa and Vendeville, 2002). The thrust spacing which is the distance between adjacent forethrusts is smaller with higher basal friction (Mandal, 1997).

1.2.2. **Related Experimental Modeling**

There are more than a dozen fold-thrust belts that are developed above evaporites (Davis and Engelder, 1987; Letouezey et al., 1995; Cotton and Koyi, 2000). A series of experimental models have been built to investigate the kinematics of thin-skinned fold-thrust belts above frictional and ductile detachments (Letouezey et al., 1995; Cotton and Koyi, 2000; Costa and Vendeville, 2002; Bahroudi and Koyi, 2003; Smit et al., 2003; Luján et al., 2006; Vidal-Royo et al., 2009).

These experiments showed that the structure of the thrust units developed above ductile detachments is different from that above frictional detachments. Above frictional detachments, imbrication of forward-verging thrusts ("forethrusts") builds up the wedge, whereas symmetrical box-folds with both forethrusts and backthrusts are predominant above the ductile detachments. (Mulugeta, 1988; Letouezey et al., 1995; Cotton and Koyi, 2000; Costa and Vendeville, 2002; Smit et al., 2003). The thrust spacing was found to be smaller with higher basal friction (Mandal, 1997).

Different structural styles can be explained by Figure 1.3 (Davis and Engelder, 1985): higher basal friction leads to higher ψ_b which is the angle between σ_1 and the

base of the wedge and results in smaller θ_f which is the dip angle of forethrusts with the base of the wedge and larger θ_b which is the dip angle of backthrusts with the base of the wedge (Figure 1.1). Therefore, with high basal friction, forethrusts are preferred because of smaller θ_f. Above low basal friction detachment, both forethrusts and backthrusts are favorable because θ_f is close to θ_b.

Cotton and Koyi (2000) used a series of sandbox experiments with lateral adjacent frictional and ductile substrates to simulate thin-skinned deformation developed in the Salt Range and Potwar Plateau in Pakistan. They controlled the initial thickness of the ductile substrate as well as the prekinematic and synkinematic overburden wedges. They concluded that deformation propagated farther and faster above a ductile substrate than above a frictional substrate, and the rate of propagation increased with increased thickness of the ductile substrate. Additionally, Bahroudi and Koyi (2003) applied similar experiments with the uneven spatial distribution of the ductile substrates to Zagros fold-thrust belt in order to study the effect of spatial distribution of Hormuz salt. Their models suggest that uneven distribution of a ductile substrate leads to an irregular deformation front with frontal and lateral ramps and variation in deformation style and strain partitioning. Similarly, Vidal-Royo et al. (2009) used two series of experiments with three isolated ductile substrates to model the formation of orogeny-perpendicular thrusts in Central External Sierras in Spain. Their results indicate that shortening is accommodated by additional uplift and penetrative strain in areas above a frictional substrate which is in between two ductile substrates.

Letouezey et al. (1995) employed sandbox experiments underlain by a ductile substrate with an oblique lateral boundary to study the control of the Triassic salt basin on the Jura fold-thrust belt. The deformation front of the structures developed above the ductile substrate is limited by the extent of the ductile substrate. On the other hand, Costa and Vendeville (2002) looked into the geometry and kinematics of fold-thrust belts above the ductile substrate specifically. They designed a series of experiments with a differential initial thickness of the ductile substrate and the presence of the deformable backstop (described as "synkinematic overburden wedge" in Cotton and Koyi, 2000) together with a frontal substrate pinch-out. They stated that models bounded by two vertical end walls always deformed by symmetric folding and thrusting while models with the thick ductile substrate and deformable backstop together with a frontal substrate pinch-out were dominated by forethrusts and asymmetric folds.

Models with along-strike variation in detachment rheology showed deflection in the deformation front between two domains, resulting in a transfer zone between the two parts (Calassou et al., 1993; Letouezey et al., 1995; Cotton and Koyi, 2000; Bahroudi and Koyi, 2003). Under the condition of across-strike variation in detachment rheology, the deformation front is found to move forward when reaching ductile detachment domain. The ductile layer was found to thicken when the deformation front reaches the frontal limit of the ductile substrate (Cotton and Koyi, 2000).

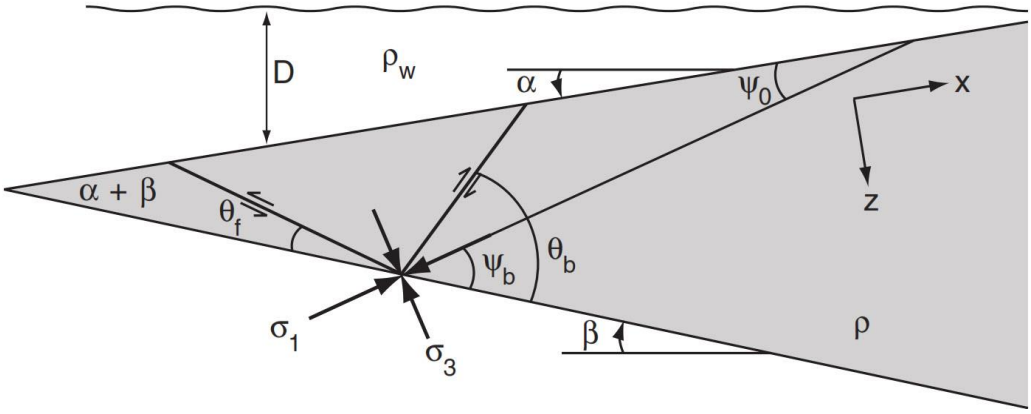

Figure 1.1: Cross-sectional sketch of a critically tapered submarine wedge (Dahlen and Suppe, 1988). α is the surface slope and β is the basal dip. σ_1 and σ_3 are the maximum and minimum compressive stresses within the wedge. ψ_b is the angle between σ_1 and the base of the wedge. The angle between σ_1 and x-axis is denoted by ψ_0. θ_f is the dip angle of forethrusts with the base of the wedge and θ_b is the dip angle of backthrusts with the base of the wedge. ρ and ρ_w are wedge density and water density. D is the local thickness of the water overburden along the direction of gravity.

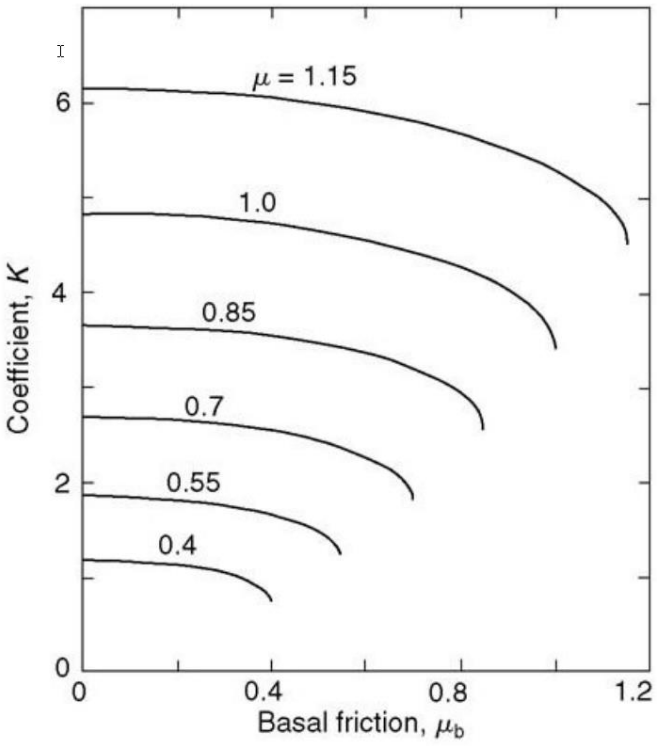

Figure 1.2: Sensitivity of coefficient K to basal and apparent internal coefficients of friction μ_b and μ (Davis et al., 1983). If μ_b is small in comparison with μ, $K \approx 2\sin\phi\,/(1-\sin\phi)$, but as $\mu_b \to \mu$, K decreases significantly and in fact $\partial K/\partial\mu_b \to -\infty$.

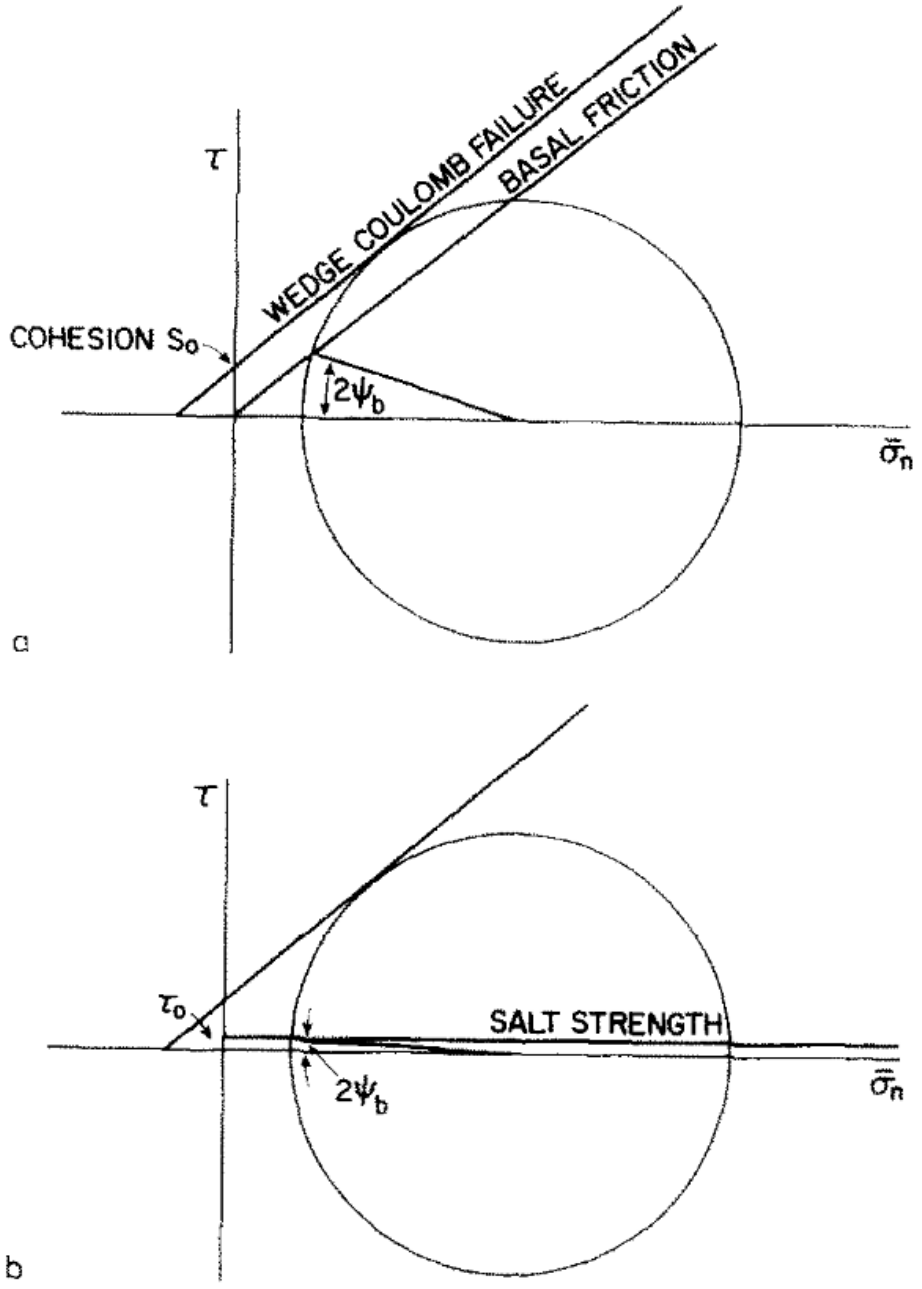

Figure 1.3: Mohr-Coulomb diagram showing the contrast in ψ_b, the dip of the axis of maximum compressive stress σ_1 with respect to the basal décollement, for (a) a strong and (b) a weak, salt décollement (Davis and Engelder, 1985).

CHAPTER 2: METHODOLOGY

2.1. ***Experimental Modeling Material***

Dry quartz sand was used as analogue materials to simulate the brittle and frictional behavior of upper crustal sedimentary rocks because sand exhibits Mohr-Coulomb behavior, and has been widely used in experimental modeling. In this study, dry quartz sand was sieved to a grain diameter of 0.15 to 0.20 mm. Transparent silicone gel was used to simulate the ductile behavior of evaporitic rocks. The silicone gel used in this study is a Newtonian material, with a kinematic viscosity of 10,000,000 cSt and a density of 1.1 g/ml. It is commonly used as an analog for salt.

2.2. ***Experimental Setup***

The experiments were run in a plexiglass sandbox designed for compressional analog experiments (Figure 2.1, 2.2). The sandbox is composed of a horizontal rigid basement, two stationary side walls, one stationary end wall and one movable plate driven by the motor. The compressional rate for all experiments was 0.5mm/min. All models had an initial width parallel to the shortening direction of 40 cm and a fixed length of 53.5 cm.

A portion of the sandbox was covered by silicone gel as the ductile substrate, and the remainder was covered by quartz sand as the frictional substrate. The extent of silicone gel varied depending on the configuration of the salt boundary being investigated in each experiment. The sand pack had several layers with two contrasting colors, white and blue, but the same mechanical properties. The top surface was imprinted with 1.27 cm (0.5 inches) square grid which served as a marker recording the surface deformation.

Six models (Figure 2.3) were designed to study four variables that may control the structural styles and map trends: (1) the geometry of the boundary of the silicone layer; (2) thickness of the silicone layer; (3) the extent and geometry of the silicone layer defining the boundary between the frictional and ductile detachments; and (4) the width of the deformable backstop. Although some of these controls have been studied by previous authors, the suite of models examined comprehensively the effects of all of the controls in more detail. The specification of the models is summarized in table 1.

Model 1. *Thin Silicone Layer and Transverse Boundary Setup*: This model investigated the nature of deformation above frictional and ductile detachments, and the nature of the deformation above a transverse boundary between the two types. A thin silicone layer was used in this model (0.5 cm). The shape of the silicone layer was rectangular, resulting in a transverse boundary between the frictional and ductile detachments. The length and the width of the silicone layer were 27 cm and 20 cm. The silicone layer was laid on the basal plate representing basement, and it was touching one of the side walls and the movable plate. Above the silicone layer, the thickness of the sand layer was 2 cm. The rest area of the sandbox was covered by the sand layer of 2.5 cm thick. The thickness ratio between the silicone layer and the overburden layer in the area with a ductile detachment was 1/4.

Model 2. *Thin Silicone Layer and Oblique Boundary Setup*: Compared to Model 1, the lateral boundary of the silicone layer was at 45° to the movable plate and the shortening direction. All other parameters were kept the same. A comparison of Model

1 and 2 showed the variation in the deformation above transverse versus oblique boundaries in the detachment surface.

Model 3. *Thick Silicone Layer and Transverse Boundary Setup*: Compared to Model 1, the silicone layer in this model was 1 cm. This model investigated the effects of a thicker ductile unit at the base on the deformation. The thickness of the sand layer above the silicone layer was 1.5 cm. The thickness of the sand layer in the remaining area was 2.5 cm. The thickness ratio between the silicone layer and the overburden layer was 2/3 in the area with a ductile detachment.

Model 4. *Thin Silicone Layer, Transverse Boundary, and Wide Silicone Layer Setup*: Compared to Model 1, the silicone layer had a greater width, thereby increasing the width of the detached fold belt. The purpose of this model was to study the difference in thrust propagation with a larger detached surface.

Model 5. *Thin Silicone Layer, Transverse Boundary, and Narrow Deformable Backstop Setup*: The size and the shape of the silicone layer were the same as the silicone layer in Model 1; however, the silicone layer was shifted forward by 10 cm. In other words, there was a 10 cm wide deformable backstop built with 2.5 cm thick sand layer. This set up investigates a fold belt with a ductile detachment in front of one with a frictional detachment, and the transition between the two styles.

Model 6. *Thin Silicone Layer, Transverse Boundary, and Wide Deformable Backstop Setup*: Compared to Model 5, the deformable backstop in this model was wider (20 cm). In this case, the silicone layer was touching one of the side walls and the stationary end wall. This model simulates a wider frictional belt behind the one with the ductile detachment.

Table 1: Summary of experimental setup for six models

Model	Silicone Gel Layer Boundary Type	Silicone Gel Layer Width	Silicone Gel Layer Thickness	Deformable Backstop Width
1	Transverse	20 cm	0.5 cm	0 cm
2	Oblique	20 cm	0.5 cm	0 cm
3	Transverse	20 cm	1 cm	0 cm
4	Transverse	30 cm	0.5 cm	0 cm
5	Transverse	20 cm	0.5 cm	10 cm
6	Transverse	20 cm	0.5 cm	20 cm

2.3. ***Boundary Conditions***

The top surface is a free surface. The shortening is produced by the movement of the vertical movable plate on the back with the velocity of 0.5 mm/min. The vertical end wall is stationary. The basement is covered by two kinds of detachments, frictional and ductile. The frictional detachment refers to the detachment between the sand pack and the basement, and the ductile detachment refers to the detachment between the silicone layer and the basement. The basal shear stress along the frictional detachment is much higher than it along the ductile detachment which is extremely low. The purpose of the side walls is to bound the system only; however, lateral shear stresses along the side walls induced edge effects on the system. Costa and Vendeville (2002) stated that the lateral shear stress applied a strong influence if the basal shear stress was proportionally low. However, as long as the affected areas are not considered as part of the analysis, the lateral shear stress is not affecting the geometry and the trend of major structures.

2.4. ***Analysis***

All models were recorded from the top by a camera with one image per 0.25 cm of shortening. For some of the models, when the experiment was finished, the surface of the final stage was scanned with a *NextEngine* 3D laser scanner to study the variation in structural relief. After the experiment, the model was covered by an additional white sand layer in order to preserve the structures, and water was sprayed into the sandbox to consolidate the sand. After a few hours, when all the sand was consolidated, the model was cut along at least five cross-sections in the direction parallel to the shortening direction. These slices were analyzed to study the variation in the cross-sectional geometry of the structures.

For top view images, around 5 cm wide areas adjacent to the side of the model where the boundary effect was pronounced based on the observation were trimmed. The trimmed images were used to develop animations showing the deformation progress. Moreover, the final image was further mapped to show the detailed geometry of forethrusts and backthrusts. The surface reference grid was considered as the marker as well as the scale. Thrust spacing, defined as the distance between adjacent forethrusts, was determined and the distance of deformation front from the movable plate at each stage was also recorded.

The 3D XYZ file of the surface created by the 3D scanner was composed of three separated XYZ files partially overlapping each other because the size of the sandbox exceed the largest area the 3D scanner was capable of scanning with a reasonable resolution. The software *ScanStudio* was used to align two overlapping XYZ files. Before the XYZ file was exported, the 3D file was polished and simplified

considering the processing capability of the 3D processing software that was used to further process the 3D file. The main part of the processing work was finished on the software *GOCAD*. Images of the processed surface were used for analyses.

Because of the edge effect of the side walls, side images were not adopted; only cross-sections cut through the main body of the model were used for analyzing the structural style and the Coulomb wedge. Cross-sections were captured as panoramic photos, so that the photos were built by stitching multiple photos. Thrusts and detachments were traced on the cross-sections based on the contrast color layers.

Top view and cross-section images analyses were conducted for all six models. 3D surface images analyses were developed for Model 3 and Model 4, which were considered as additional information for top view images.

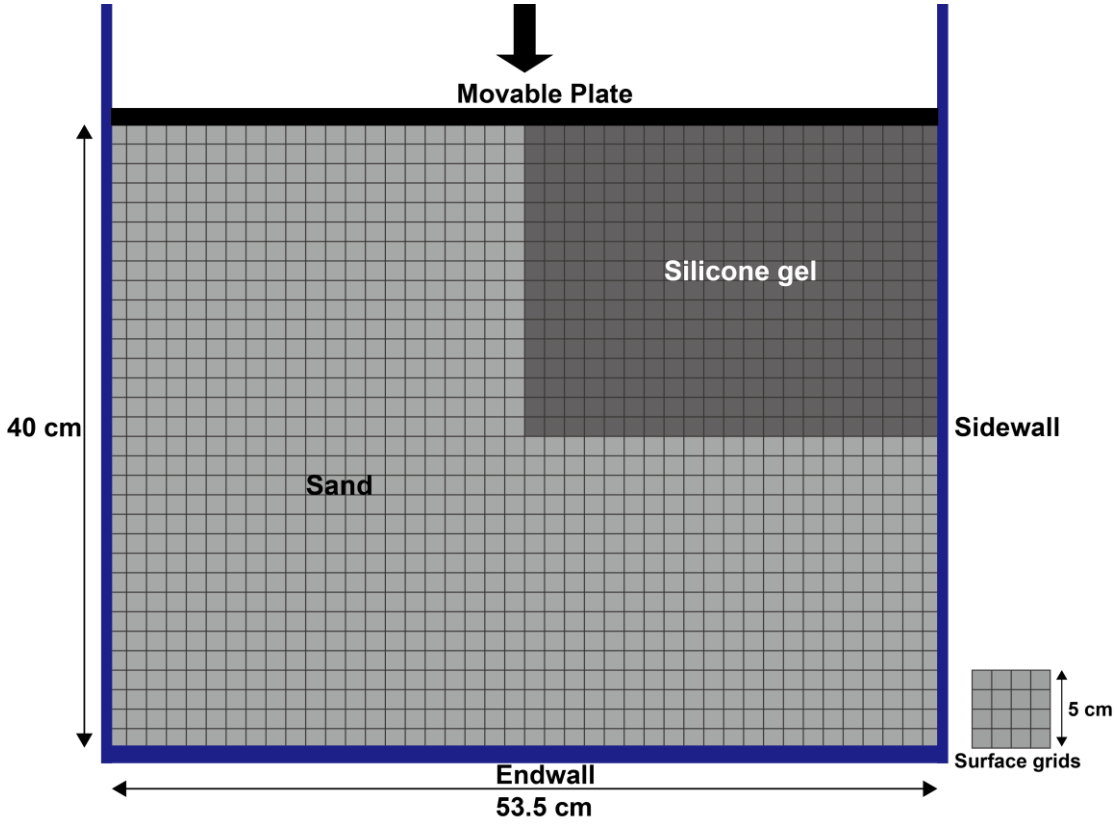

Figure 2.1: Line drawing of the map view of the sandbox showing the movable plate and fixed frontal end wall and side walls. The shortening direction is labeled as the arrow. The location of the sand and silicone, as well as the surface grids, are drawn in.

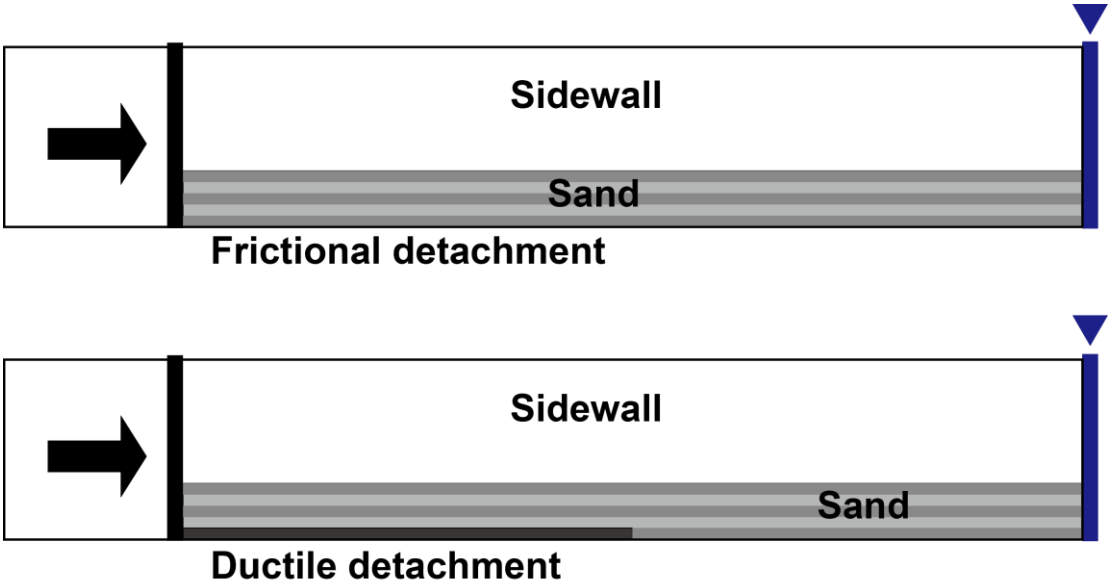

Figure 2.2: Line drawing of two cross-section views of two different detachment domains. The movable plate and the end wall are on the horizontal basement. The shortening direction is shown by the arrow.

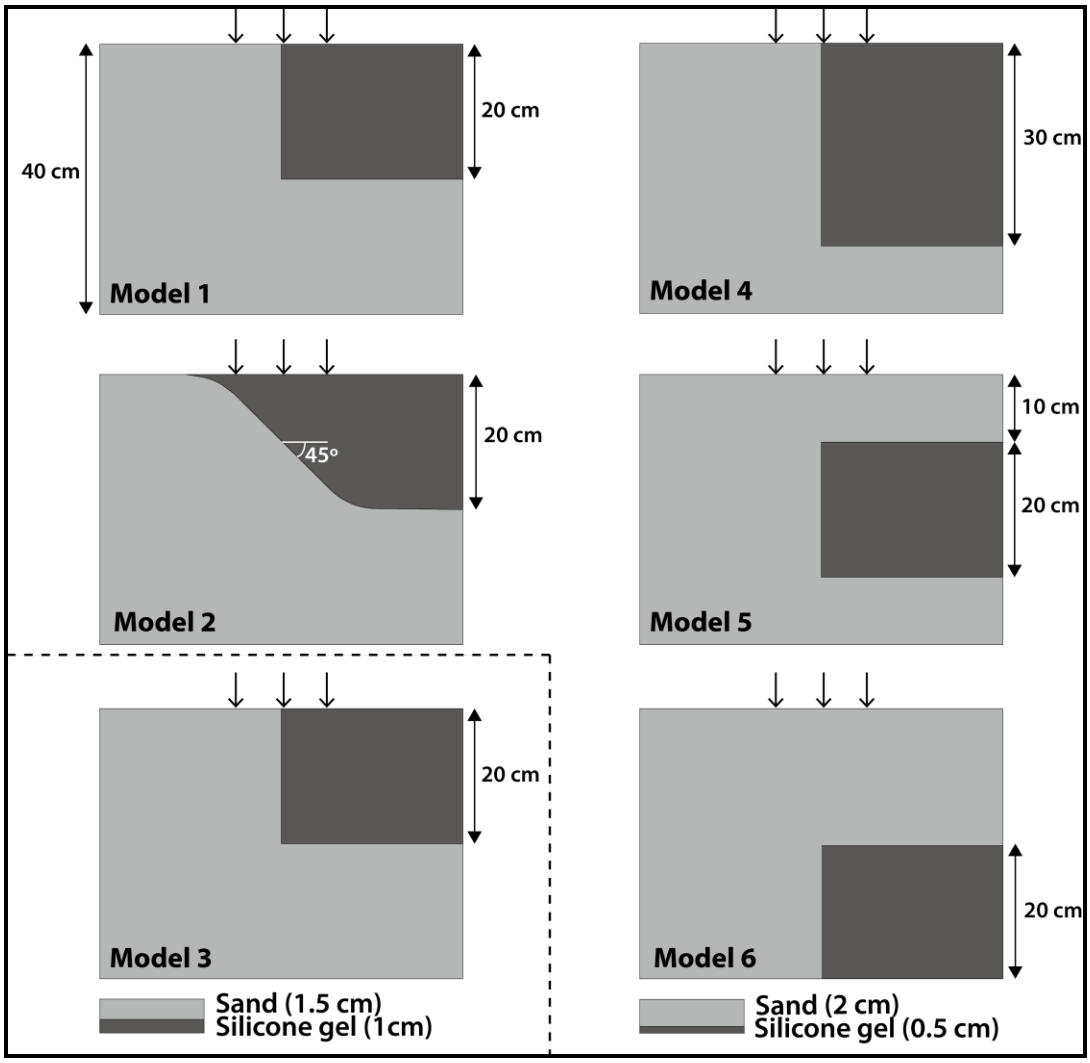

Figure 2.3: Line drawing of the map view of the experimental setup with the configuration of the silicone layer with arrows indicating shortening direction. Dark grey blocks indicate areas underlain by the silicone gel. Model 1: Thin silicone layer and transverse boundary setup. Model 2: thin silicone layer and oblique boundary setup. Model 3: Thick silicone layer and transverse boundary setup. Model 4: Thin silicone layer, transverse boundary, and wide silicone layer setup. Model 5: Thin silicone layer, transverse boundary, and narrow deformable backstop setup. Model 6: Thin silicone layer, transverse boundary, and wide deformable backstop setup

CHAPTER 3: RESULTS AND ANALYSES

3.1. *Map and Cross-Sectional Geometries*

The results and analyses of each experimental setup will be discussed using both the evolution and final geometry in map view, and the cross-sectional geometry in a series of cross-sections. Because the experiments share a number of common properties, the basic geometry and evolution are mainly discussed for Model 1, and subsequent discussions of additional models focus on the main differences resulting from the changes in the experimental configurations.

3.1.1. **Model 1**

(A) Structural Evolution

Nine stages of the experiment are shown in Figure 3.1A-I. The interval between the stages is 1 cm of shortening. As the moveable plate moved forward, thrusts perpendicular to the shortening direction were developed sequentially from the hinterland towards the foreland. This kind of forward fold-thrust propagation pattern is consistent with Davis et al. (1983)'s conclusion that the Coulomb wedge deforms until a critical taper is attained, after which it continues to grow at constant taper as additional material is encountered at the toe. The first two thrusts developed above the frictional detachment were at approximately the same distance from the back wall as those above the ductile detachment; however, at 3 cm of shortening (Figure 3.1D), the third thrust above the ductile detachment nucleated at a large distance from the second thrust, and a related backthrust also formed. At 4 cm of shortening (Figure 3.1E), the third thrust above the ductile detachment curved back and connected with the frontal thrust in the frictional detachment domain. With continuing deformation, a few more

closely-spaced thrusts were developed above the frictional detachment while another forethrust-backthrust pair were developed above the frontal end of the silicone layer in a more forward position. All of these frontal thrusts underwent a sharp bend at the transition zone as they connected with corresponding thrusts above the frictional detachment. The frontal structure above the ductile detachment was limited by the frontal boundary of the silicone layer. The very frontal thrust above the frictional detachment developed at a much larger spacing than all of the other thrusts. Its location appears to be controlled by the lateral propagation of the frontal thrust above the ductile detachment.

(B) Final Geometry

The tracing of both forethrusts and backthrusts is shown in the final stage is shown Figure 3.2. In general, the thrust spacing, the distance between the newly formed thrust and the thrust behind it, was larger in the ductile detachment domain than the thrust spacing in the frictional detachment domain. The last thrust developed above the frictional detachment is an exception considering the typical thrust spacing in the frictional detachment domain, and this phenomenon will be discussed later in the statistical analysis of sequential top view images.

There was a clear difference in the structural style above the frictional and the ductile detachments. The frictional detachment was characterized by closely-spaced forethrusts (black), whereas the ductile detachment was characterized by forethrusts (black) and backthrusts (red), with the backthrusts terminating at the boundary of the ductile detachment. Thrusts on either side connected along a fault zone at a very high angle to the regional trend at the lateral boundary of the silicone layer.

Serial cross-sections provided additional information on the fold-thrust geometries and the transition in structural styles. In sand models, the thrusts are represented by shear zones instead of clean fault planes, so that the exact locations and terminations of the faults are difficult to determine. Above the frictional detachment, the structure was characterized by piggy-back imbricates of forethrusts forming duplexes made up of systems of fault-bend folds. The result was consistent with the top view observation, which shows closely spaced forethrusts. Davis and Engelder (1985) explained, with strong basal detachment, the dip of the forethrusts was shallower than the dip of the backthrusts, which was why forethrusts were more common than backthrusts in most thrust belts and accretionary prisms.

In the ductile detachment domain, symmetric box folds with both forethrusts and backthrusts developed dominated the structure. Based on Mitra's (2003) unified kinematic model for the development of detachment folds, the symmetric to asymmetric box folds developed in this case can be classified as detached disharmonic to lift-off folds. The wavelength (~7 cm) of the detachment folds was generally the same among other models with the same sand/silicone thickness ratio. The detachment folds also show both across and along trend with the same fold exhibiting an along-trend change from symmetric to asymmetric geometries and vergence direction.

In the transition zone between the two types of detachments (e.g. Figure 3.3D), the cross-sections shared features of structural styles of both types. Typically, forward-verging detachment folds were exhibited.

3.1.2. **Model 2**

(A) Structural Evolution

The primary difference in the setup between Model 2 and Model 1 was that the silicone-sand boundary was at an angle of 45° to the movable plate in Model 2. The evolution of structures in Model 2 is shown at nine selected stages in Figure 3.4A-I for each centimeter of shortening. The first thrust was subparallel to the movable plate. At 3 cm of shortening (Figure 3.4D), the first backthrust and the second forethrust above the ductile detachment nucleated, as did one above the frictional detachment. Similar to Model 1, the second forethrust above the silicone layer was at a large distance from the first thrust compared to the second thrust developed in the frictional detachment domain. The geometry of the second and third forethrust in the ductile detachment domain followed the boundary of the silicone layer underneath it. The thrusts above the frictional detachment were closely spaced and connected to those in the ductile detachment domain along an oblique forethrust in the transition zone. The orientation of this forethrust was controlled by the oblique boundary of the ductile detachment.

(B) Final Geometry

The Figure 3.5 shows the final stage of the experiment with forethrusts and backthrusts mapped. As expected, the thrust spacing in the ductile detachment domain was larger compared to the thrust spacing in the frictional detachment domain. As in Model 1, only forethrusts were developed in the frictional detachment domain while both forethrusts and backthrusts nucleated above the ductile detachment

Compared to Model 1 where the lateral boundary of the silicone layer was perpendicular to the movable plate, the thrust front at the transfer zone between the frictional detachment and ductile detachment was at a smaller angle to the movable

plate in Model 2 since the lateral boundary of the silicone layer was at 45° to the movable plate. It further confirmed that the geometry of the boundary of the structure is strongly controlled by the boundary of the silicone layer at the base.

Cross-sectional images (Figure 3.6A-G) confirmed the different structural styles in the two domains observed in Model 1. Because of the wider transfer zone, a number of the cross-sections show the transition and interference between the two styles.

3.1.3. **Model 3**

(A) Structural Evolution

This model has an identical setting as Model 1, except for the larger thickness silicone/sand thickness ratio. Eight stages representing seven segments of shortening of Model 3 are shown in Figure 3.7A-H. The propagation style remained the same as the previous two models. The deformation front above the ductile detachment propagated farther forward than the deformation front above the frictional detachment. However, the thrust spacing in the ductile detachment domain was smaller than it in the previous two models.

(B) Final Geometry

The top view of the final stage with thrusts mapped on is shown in Figure 3.8. There were a number of forethrusts developed above the ductile detachment and fewer backthrusts that propagated to the surface. In the frictional detachment domain, only forethrusts were developed, as expected. The deformation front is marked by a sharp bend at the lateral boundary of the silicone layer.

Serial cross-sections (Figure 3.10A-G) show that the primary difference in the ductile detachment structures is that the structural style exhibited in this case was more asymmetric, with forethrusts and kinks-dominated structures. This style was similar to what was documented by Costa and Vendeville (2002) (Figure 3.11). They attributed the style to a thick ductile layer, a backstop behind the belt, and a progressive pinch-out of the ductile unit in the foreland, which were characteristics of their model. In the absence of the second two factors, we can conclude that the primary reason for this style is the thicker ductile unit which effectively separates the deformation in the upper sand units from the thicker ductile layer. The frictional detachment domain shows a closer thrust spacing and a larger number of thrusts than Model 1, possibly resulting from the influence of the thrust spacing in the ductile domain.

The 3D surface elevation model of the final stage of the experiment shows that the elevation contours exhibit a high relief structure with a steep wedge above the frictional detachment in contrast to the wider, low relief and narrower wedge in the ductile detachment domain.

3.1.4. **Model 4**

(A) Structural Evolution

This experiment had a wider silicone layer (30cm) compared to Model 1(20 cm). Twelve selected stages of the experiment are shown in Figure 3.12A-L. The evolution of the early few thrusts was very similar to the evolution of the structures in Model 1. The deformation front in the ductile detachment domain propagated faster and farther than the deformation front in the frictional detachment domain. The thrust spacing between the thrusts above the frictional detachment was small compared to

the thrust spacing on the ductile detachment side. Additionally, because the silicone layer in this model was wider, another pair of forethrust and backthrust were developed above the ductile detachment, so that the fold belt was wider. This experiment shows that the width of the fold belt is related to the width of the ductile detachment layer, with the frontal structure nucleating at the termination of the silicone.

(B) Final Geometry

The final stage of Model 4 is shown in Figure 3.13. The results were identical in structural style with the results in Model 1. Both forethrusts and backthrusts were observed in the ductile detachment domain while only forethrusts were developed above the frictional detachment. The last forethrust-backthrust pair in the ductile detachment domain was developed on top of the frontal edge of the silicone layer, so that the width of the fold belt is controlled by the extent of the silicone layer. The cross-sectional geometry (Figure 3.15A-G) also shows styles very similar to Model 1, except that there are a larger number of folds above the ductile detachment.

Figure 3.14 is showing the 3D surface elevation model of the final stage of the experiment from different angles. The wedge developed in the frictional detachment domain was steeper and relief of the top of the structure was higher. The structures above the ductile detachment extended over a greater distance resulting in a wider fold belt and a narrower taper than in Model 1.

3.1.5. **Model 5**

(A) Structural Evolution

This model had a narrow deformable backstop with a frictional detachment behind a zone of 20 cm wide with the silicone layer. Nine stages of the experiment

are shown in Figure 3.16A-I. The first two thrusts evolved across the entire belt with the faulted style typical of a frictional detachment. After the first two thrusts reached the silicone gel, a new forethrust developed above the ductile detachment. This forethrust propagated laterally and bent back and connected with the corresponding thrust above the frictional detachment. A backthrust above the ductile detachment nucleated and propagated in front of the first two thrusts in the backstop. The deformation front connecting the thrusts on either side had a lower angle than in Model 1. The last thrust in the frictional domain nucleated at a different interval to the previous ones (Figure 3.16H).

Unlike Model 1, the last thrust above the ductile detachment in this model nucleated behind the frontal edge of the silicone layer. Compared to Model 4, the width of the belt was narrower even though the distance between the frontal boundary of the silicone layer and the movable plate was the same.

(B) Final Geometry

The final stage of Model 5 is shown in Figure 3.17. Together with observation from the serial cross-sections (Figure 3.18A-G), the only difference from Model 1 was the presence of a narrow faulted belt consisting of duplex structures behind the detachment fold belt in the ductile domain.

3.1.6. **Model 6**

(A) Structural Evolution

This model had a much wider deformable backstop behind the silicone layer which had the same width as in Models 1 and 5. The evolution of structures in Model 6 is shown by fourteen selected stages in Figure 3.19A-N. Closely spaced forethrusts

parallel to the movable plate were developed across the sandbox until the structure reached the back end of the silicone layer. Subsequently, the new forethrust above the ductile detachment was at a large distance from the previous thrust, and was accompanied by the formation of a backthrust, which propagated into the frictional detachment domain. An additional pair of forethrust and backthrust nucleated above the ductile detachment following the formation of a few forethrusts.

(B) Final Geometry

The final stage of Model 6 (Figure 3.20) exhibits a stacked wedge of thrust faults in the deformable backstop behind a detachment fold belt in the area with the silicone layer. In the frictional detachment domain, the entire belt is made up of a duplex wedge. In addition, a major backthrust that separates the two deformation styles in the ductile detachment domain extends into the frictional fold belt resulting in a thickened wedge. These features are also observable in the cross-sectional views (Figure 3.21A-G).

3.2. ***Statistical Analyses of Sequential Top View Images***

In addition to the top view image analysis, the measurement of the distance from the movable plate to the deformation front in both domains was plotted versus the shortening distance (Figure 3.22). Moreover, Table 2 is built to summarize the measurements as well as the calculations. The plots and the data in Table 2 confirmed that the deformation above the ductile detachment (orange circle lines) propagated farther and faster than the deformation above the frictional detachment (blue diamond lines).

The reason for the faster deformation propagation in the ductile detachment domain was that the deformation front moved forward a larger distance above the ductile detachment at the time of formation of a new frontal thrust. Each jump of the orange line in the plot represents a nucleation of a forethrust. The same illustration applies to the blue lines, whereas the change in the distance of deformation front from the rear wall was less noticeable.

Comparing the plot of Model 3 (Figure 3.22C) with the plot of Model 1 (Figure 3.22A), the deformation above the ductile detachment in Model 3 propagated faster. For example, at the shortening of 4 cm, the distance of deformation front from the rear wall in Model 3 was 18 cm, while the distance in Model 1 was 13 cm. The calculated average propagation rate shown in Table 2 is also showing a higher propagation rate for the deformation above the ductile detachment in Model 3. Therefore, an increase in the thickness of the ductile layer increased the propagation rate of the deformation.

Moreover, for the later stage of Models 1, 2, 4, and 5, newly formed thrusts above the frictional detachment nucleated at a much greater distance from the previous thrusts. This dramatic change in the thrust spacing has not been mentioned by other similar analogue modeling studies. To study the causes of this phenomenon, a sandbox experiment similar to Model 1, but without the silicone layer, was designed and run. Even with a longer shortening than the shortening of Model 1, no obvious changes in the thrust spacing was noticed. Therefore, it is safe to conclude that the change in the thrust spacing above the frictional detachment was related to the influence of the ductile detachment domain adjacent to it. When the lag between the two deformation fronts on either side became larger and reached a critical distance, the deformation

front in the frictional detachment propagated laterally from the earlier-formed deformation front in the ductile domain.

Between the nucleation of two adjacent thrusts, the distance of deformation front from the movable plate decreases gradually at a constant slope. This decrease is due to the deformation of the wedge. The deformation front jumps forward when a new forethrust nucleates, which represents the point at which critical taper has been reached after an internally shortening (Davis et al., 1983). As mentioned by Mulugeta (1988), the model wedges did not exhibit steady-state features as suggested by the critical wedge taper analysis (e.g., Davis et al., 1983; Dahlen, 1990). Instead, the wedge accretes episodically. Mulugeta and Koyi (1992) explained that such a stick-slip mode of décollement propagation was thought to require less energy than sustained movement integrated over the entire décollement surface (e.g., Oldham, 1921; Gretener, 1981).

		Deformation Front Distance (cm)	Average Propagation Rate (cm per cm of shortening)	Structural Style	Typical Thrust Spacing (cm)	Changes in Thrust Spacing at Late Stages (Yes or No)
Model 1	F	14.3	1.8	Duplexes with imbricates of forethrusts	1	Yes
	D	17.8	3.6	Box folds with both forethrusts and backthrusts	5	
Model 2	F	11.5	1.9	Duplexes with imbricates of forethrusts	1	No
	D	17.4	3.2	Box folds with both forethrusts and backthrusts	6	
Model 3	F	11.8	1.8	Duplexes with imbricates of forethrusts	1	No
	D	18.5	5.1	Asymmetrical detachment folds dominated by forethrusts	4.5	
Model 4	F	17.9	1.7	Duplexes with imbricates of forethrusts	1	Yes
	D	23.4	2.5	Box folds with both forethrusts and backthrusts	6	
Model 5	F	14.7	2.1	Duplexes with imbricates of forethrusts	1	Yes
	D	22.6	3.8	Frictional thrusts behind symmetrical detachment folds	7	
Model 6	F	18.8	1.6	Imbricates of forethrusts separated by a backthrust	1.5	Yes
	D	25.6	2.2	Imbricates of forethrusts behind detachment folds	6.5	

Table 2: Summary of measurements and analyses for six models. “F” stands for frictional detachment domain; “D” stands for ductile detachment domain. Deformation front distance is represented by the farthest distance the deformation front has reached. The average propagation rate is calculated at the time the deformation front above the ductile detachment reached the farthest distance. Typical thrust spacing is estimated using the plots on Figure 3.22.

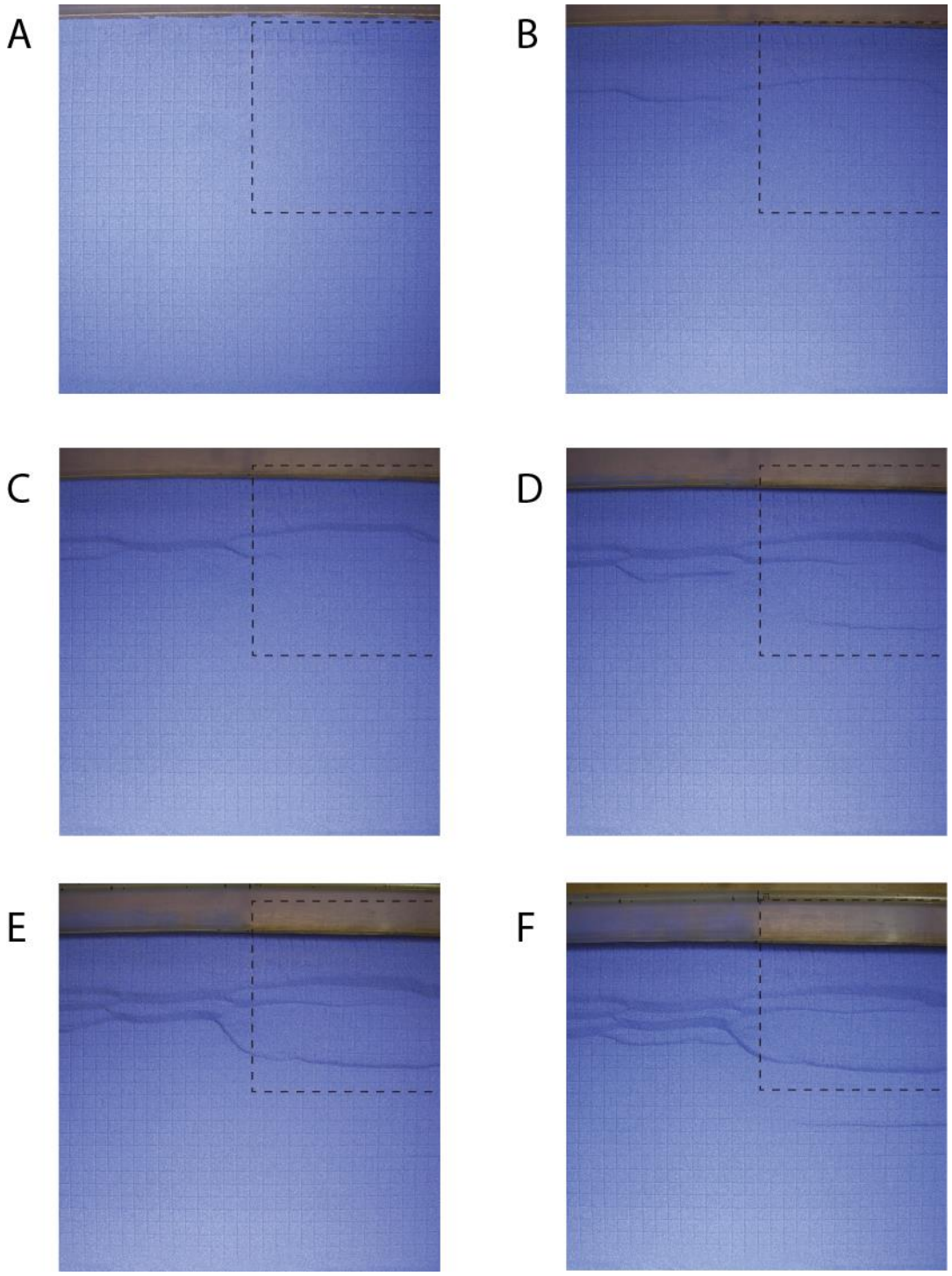

Figure 3.1: Series of selected top view images of Model 1 at incremental shortening of (A) 0 cm, (B) 1 cm, (C) 2 cm, (D) 3 cm, (E) 4 cm, (F) 5 cm, (G) 6 cm, (H) 7 cm and (I) 8 cm. The boundary of the silicone gel is indicated by the black dashed line.

G

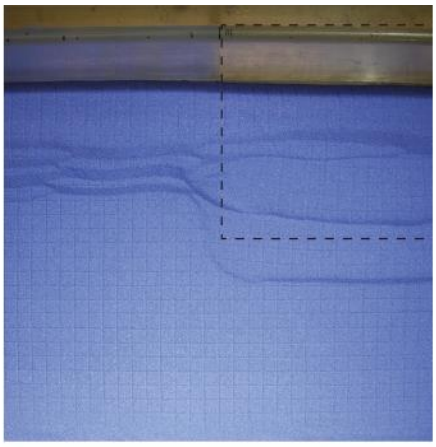

H

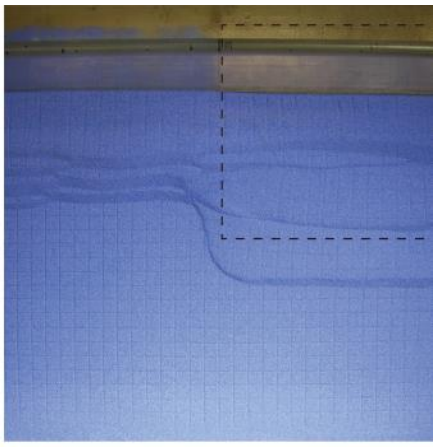

I

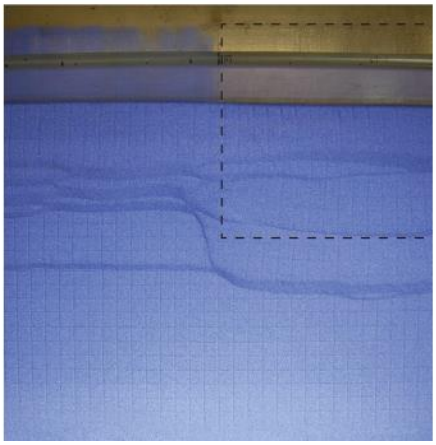

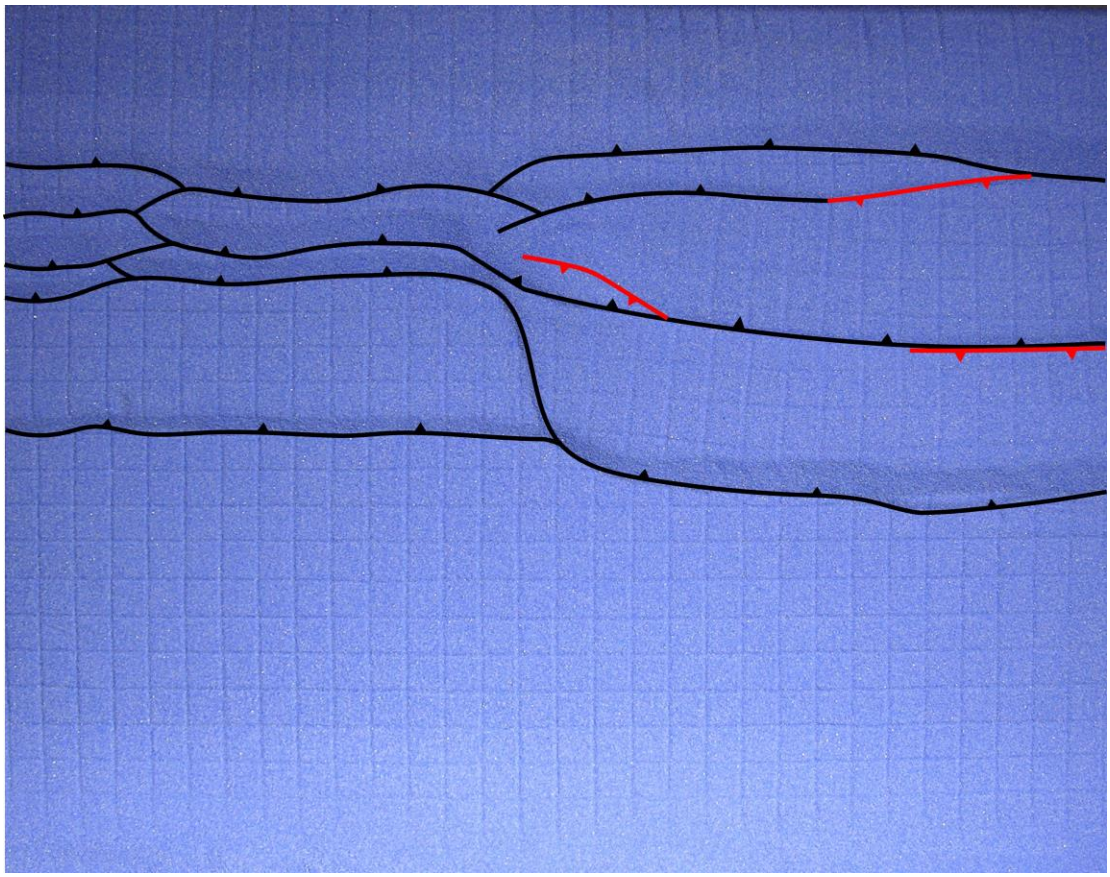

Figure 3.2: The top view image of the final stage of Model 1. Forethrusts are traced using black lines with teeth on hanging wall. Backthrusts are traced using red lines with teeth on hanging wall.

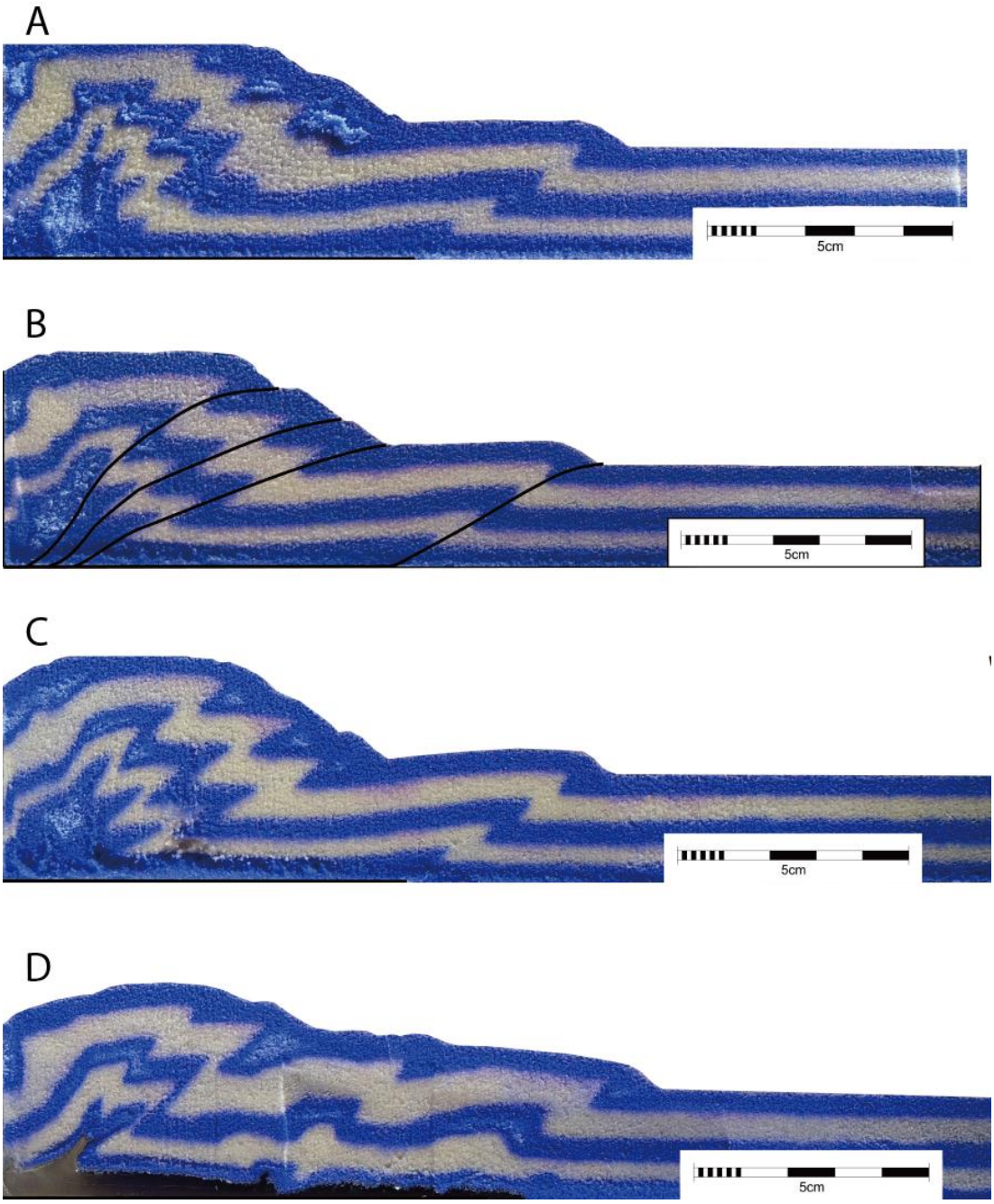

Figure 3.3: Series of cross-sectional images of Model 1. The location of each cross-section is labeled on the final stage top view image at the end.

E

F

G

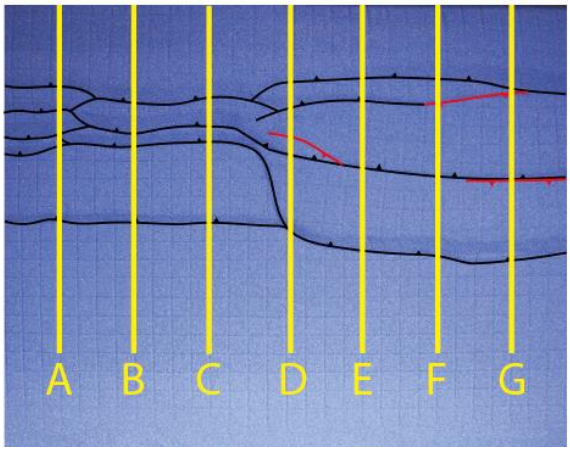

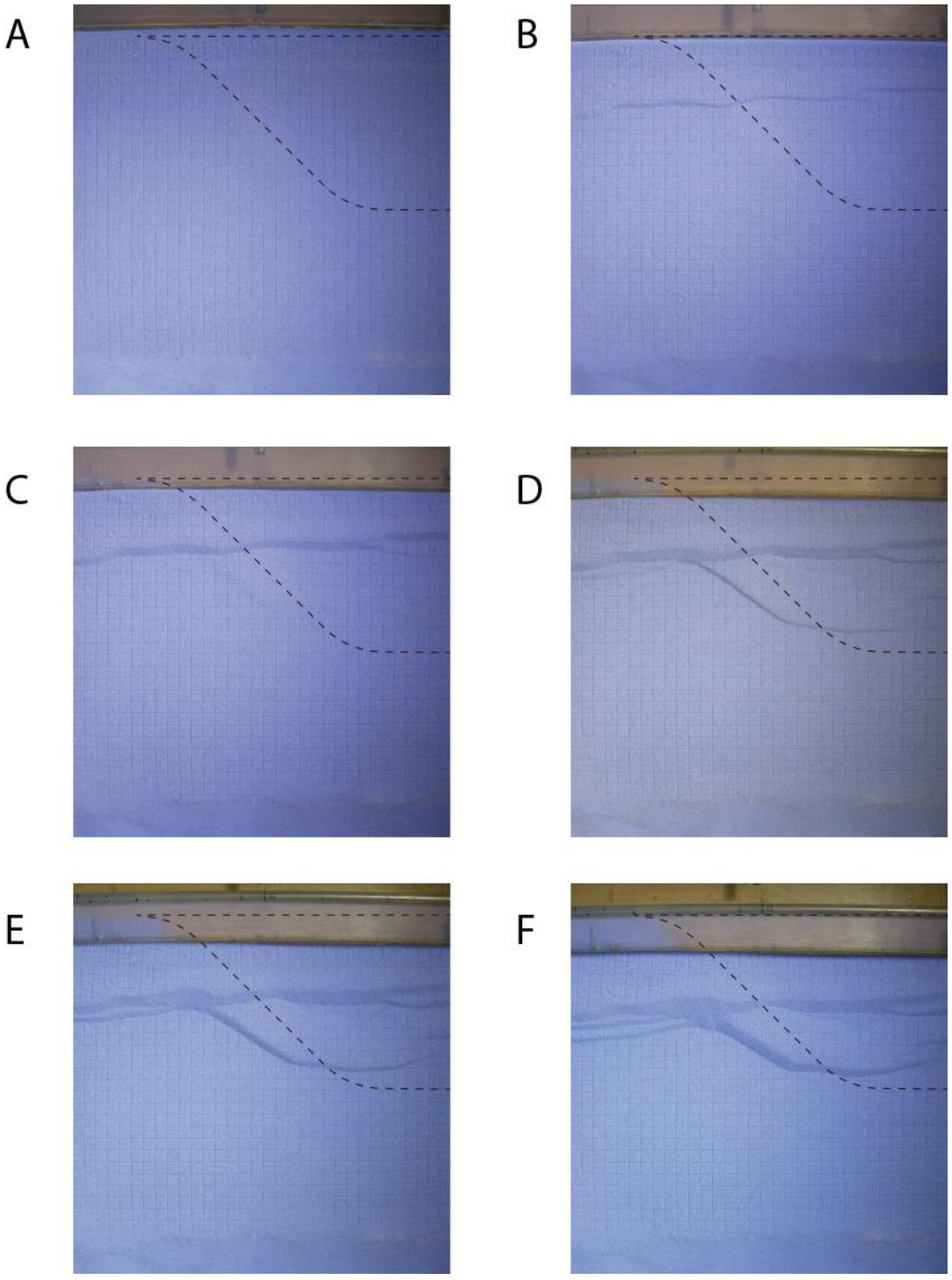

Figure 3.4: Series of selected top view images of Model 2 at incremental shortening of (A) 0 cm, (B) 1 cm, (C) 2 cm, (D) 3 cm, (E) 4 cm, (F) 5 cm, (G) 6 cm, (H) 7 cm and (I) 8 cm. The boundary of the silicone gel is indicated by the black dashed line.

G

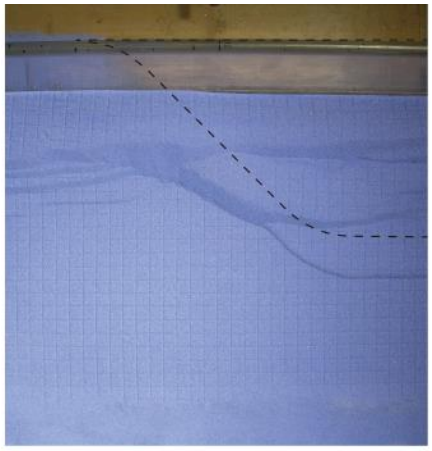

H

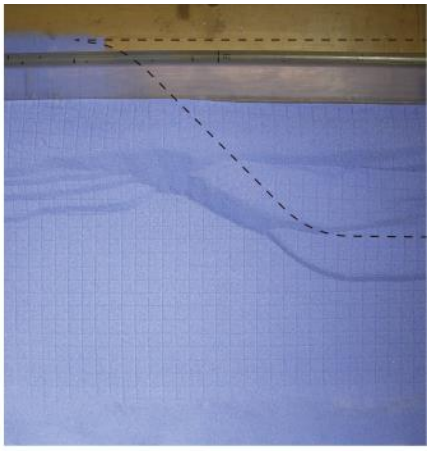

I

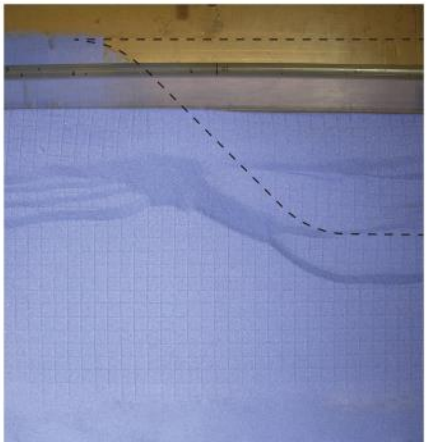

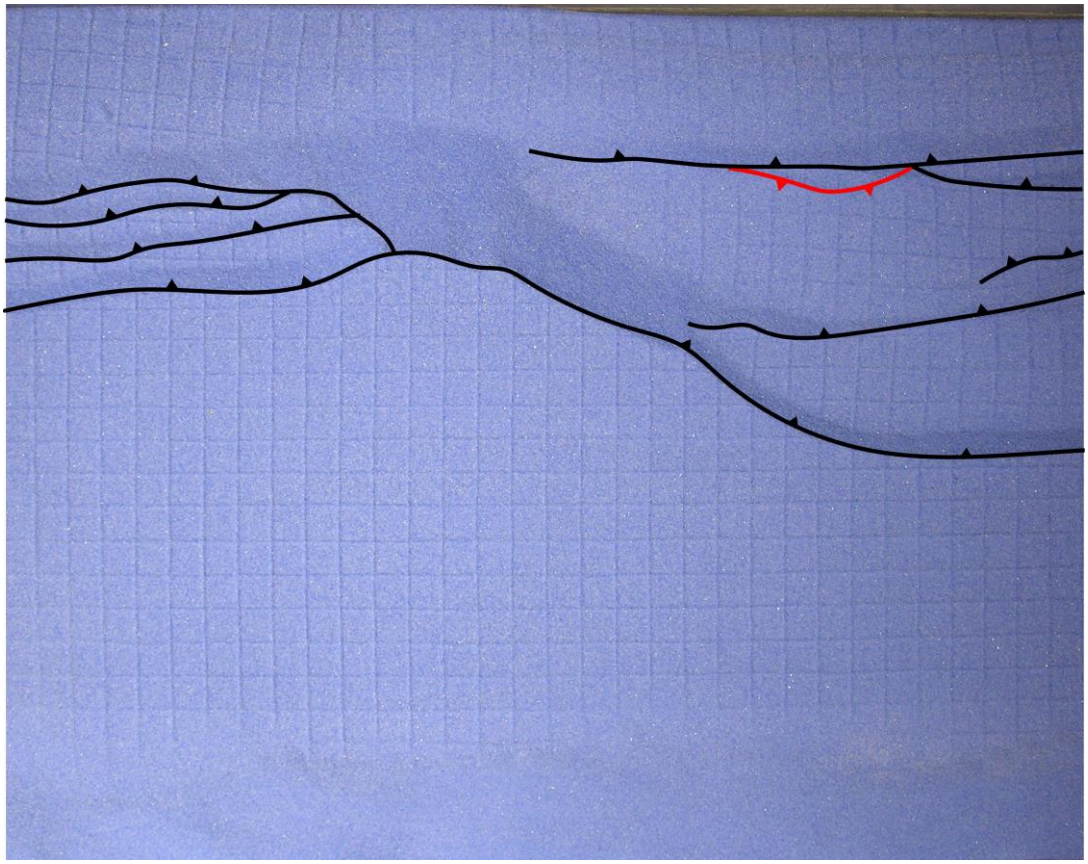

Figure 3.5: The top view image of the final stage of Model 2. Forethrusts are traced using black lines with teeth on hanging wall. Backthrusts are traced using red lines with teeth on hanging wall.

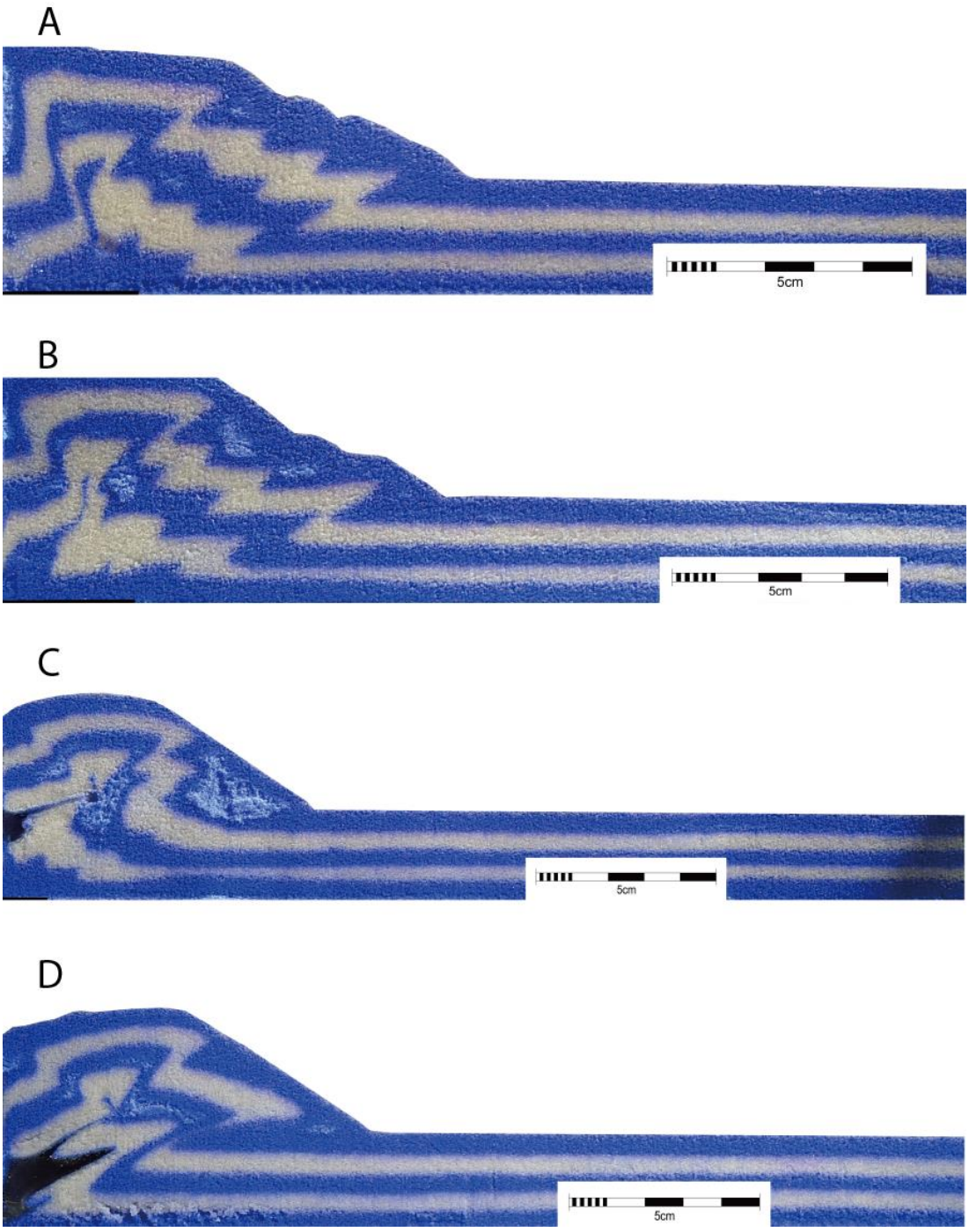

Figure 3.6: Series of cross-sectional images of Model 2. The location of each cross-section is labeled on the final stage top view image at the end.

E

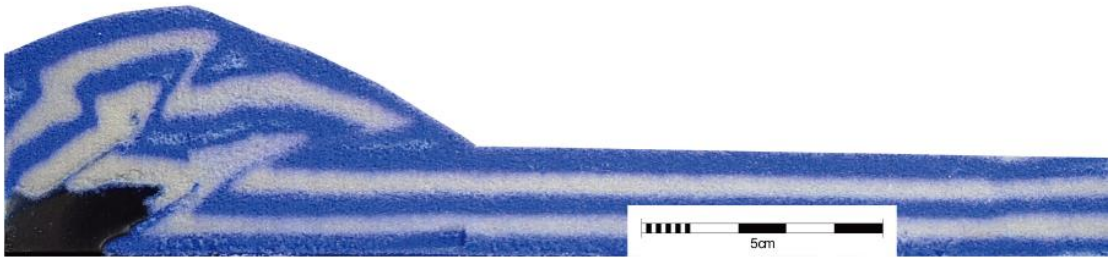

F

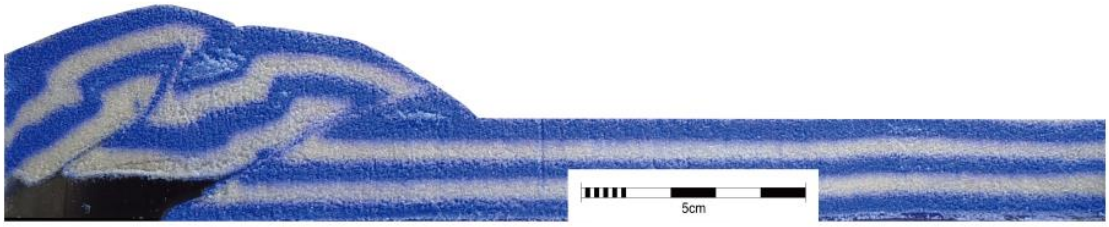

G

H

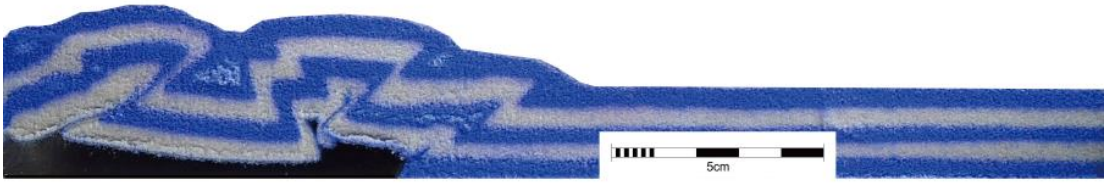

I

J

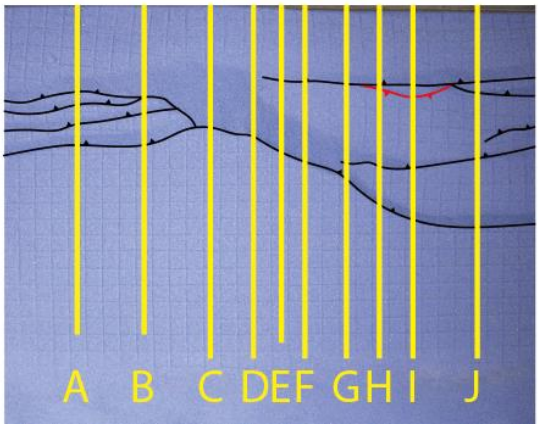

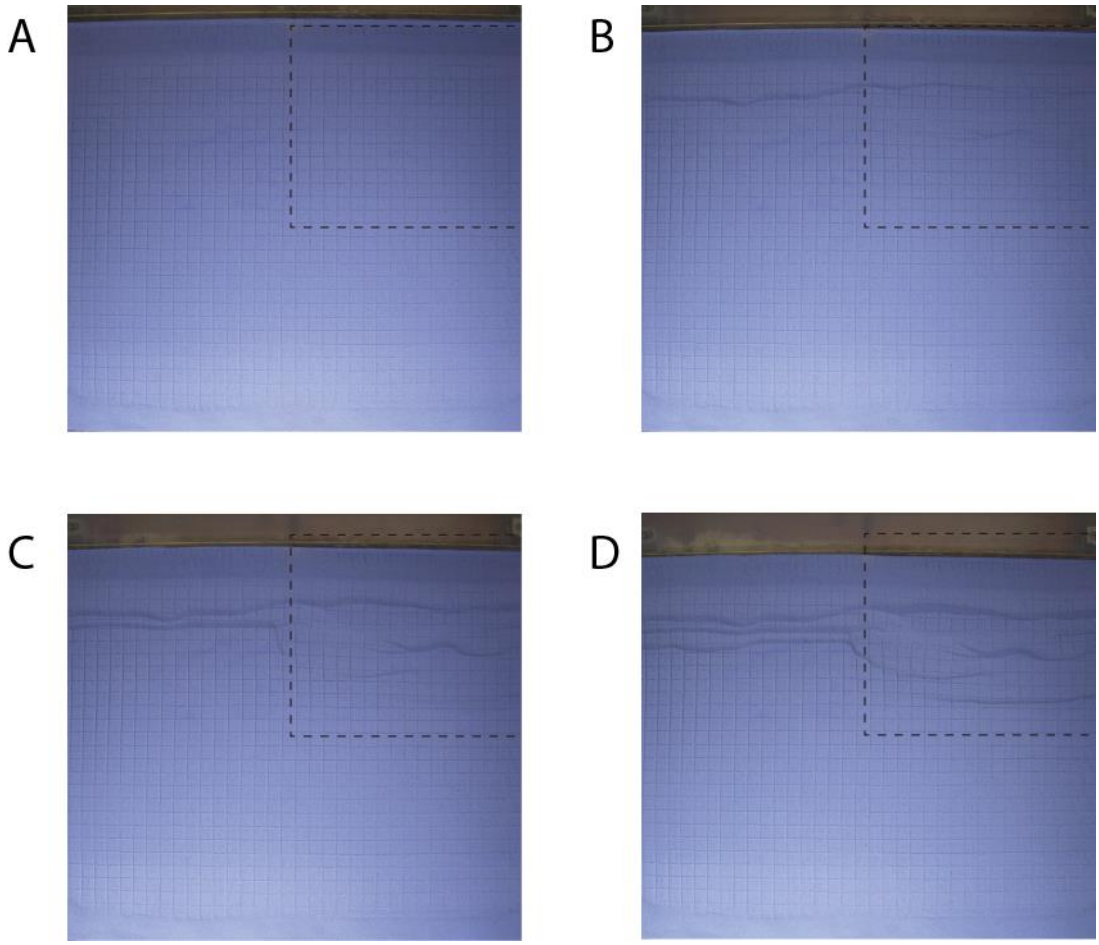

Figure 3.7: Series of selected top view images of Model 3 at incremental shortening of (A) 0 cm, (B) 1 cm, (C) 2 cm, (D) 3 cm, (E) 4 cm, (F) 5 cm, (G) 6 cm and (H) 7cm. The boundary of the silicone gel is indicated by the black dashed line.

E

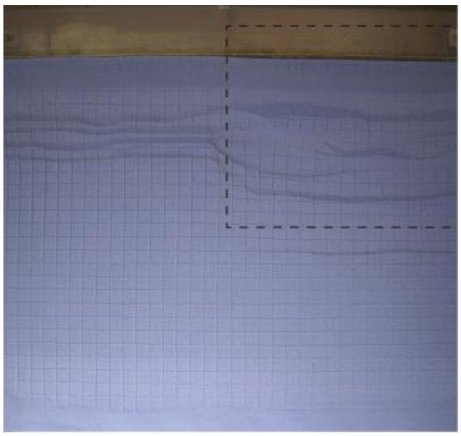

F

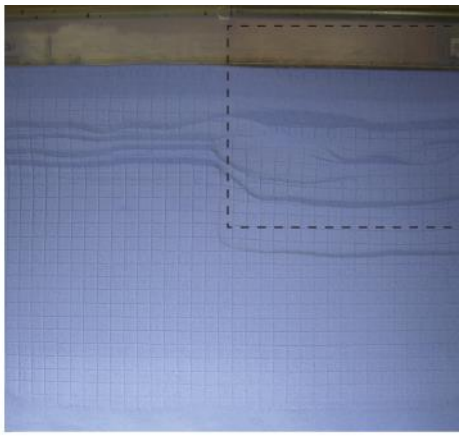

G

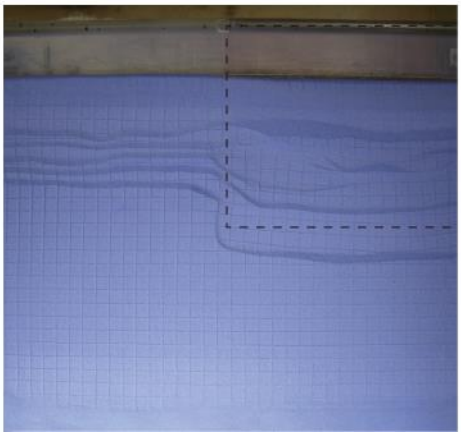

H

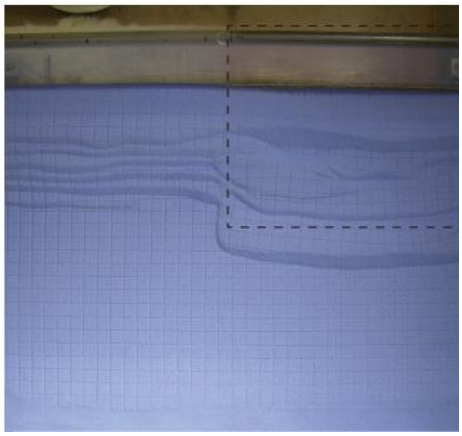

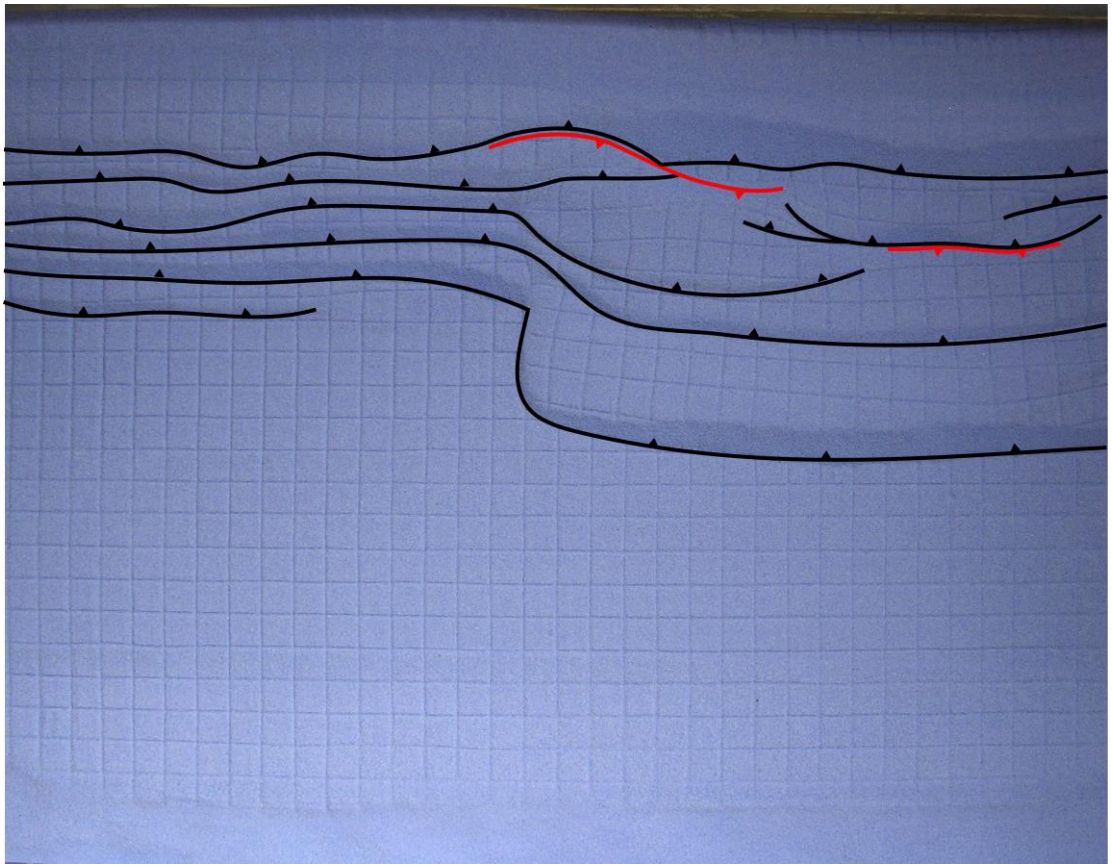

Figure 3.8: The top view image of the final stage of Model 3. Forethrusts are traced using black lines with teeth on hanging wall. Backthrusts are traced using red lines with teeth on hanging wall.

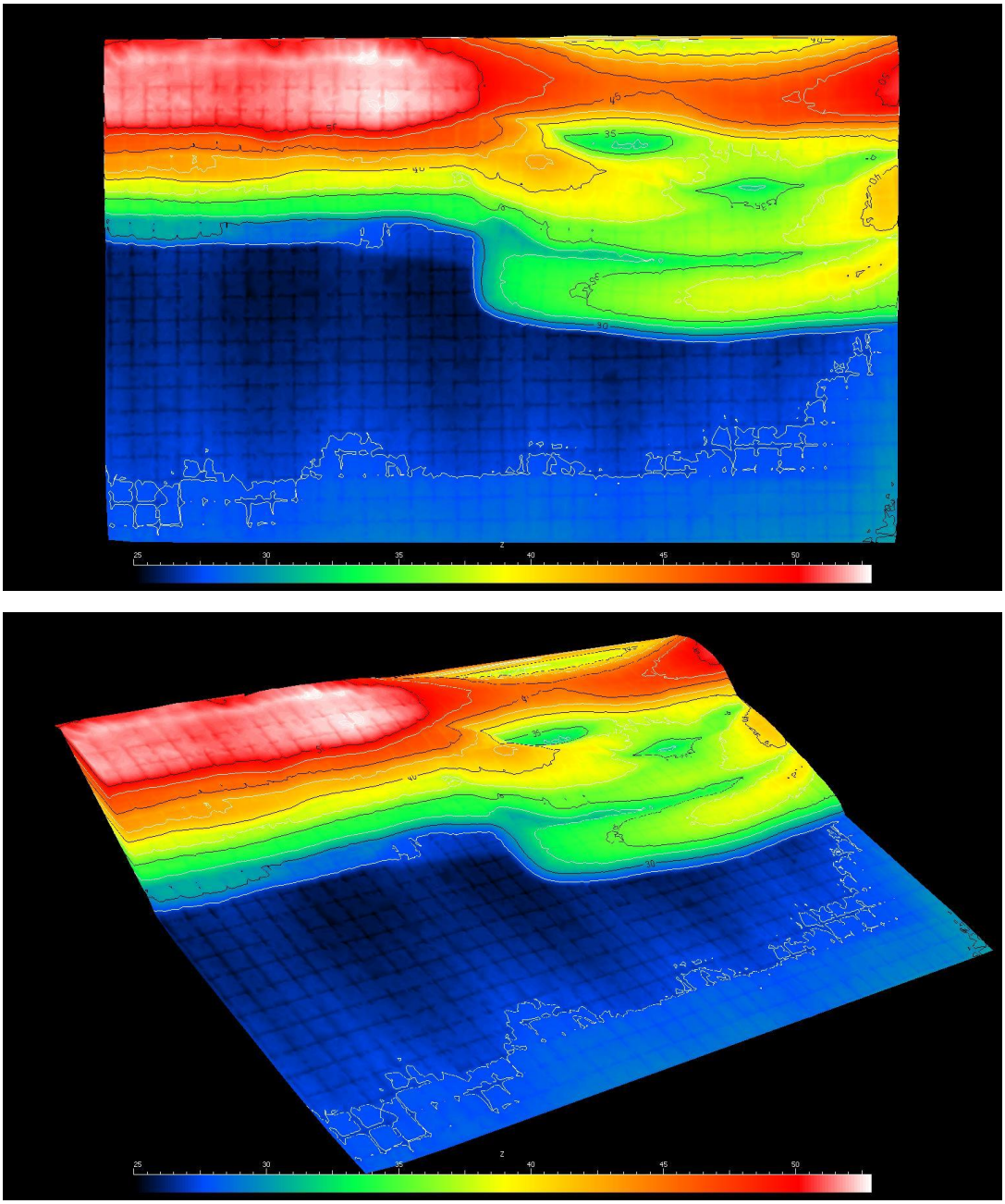

Figure 3.9: 3D scanner images of the final stage of Model 3 showing the elevation from two angles. Unit in the color bar is mm.

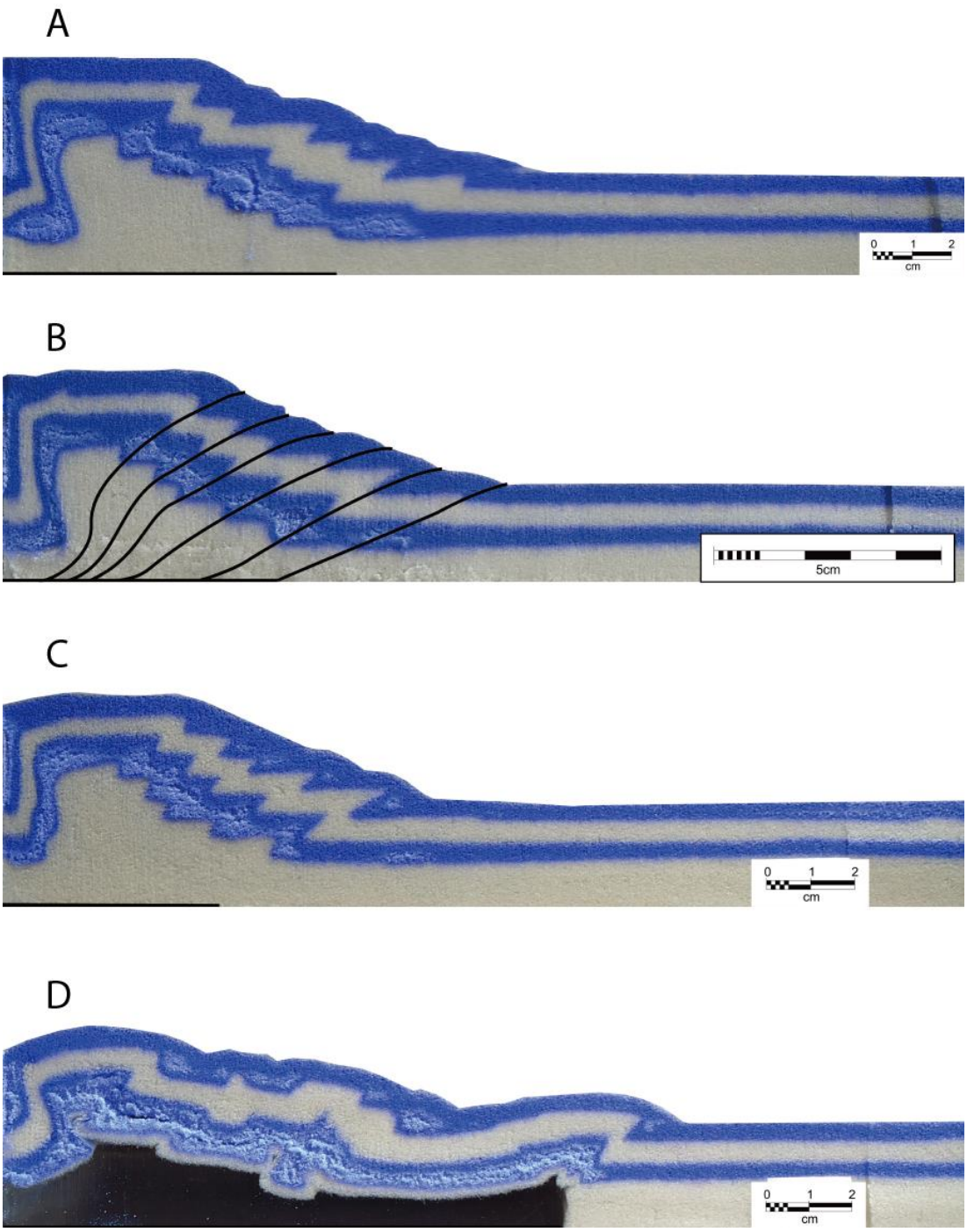

Figure 3.10: Series of cross-sectional images of Model 3. The location of each cross-section is labeled on the final stage top view image at the end.

E

F

G

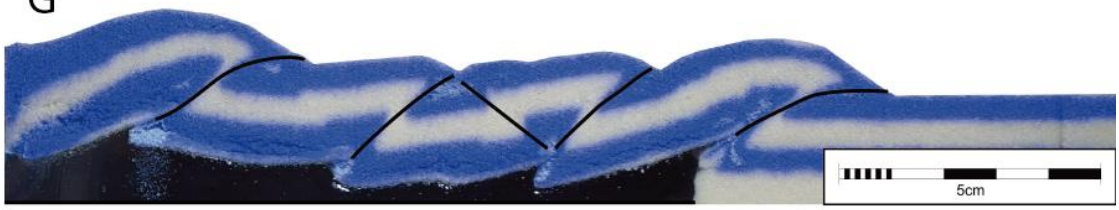

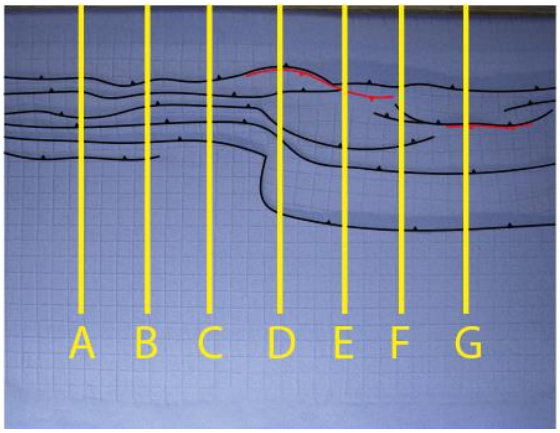

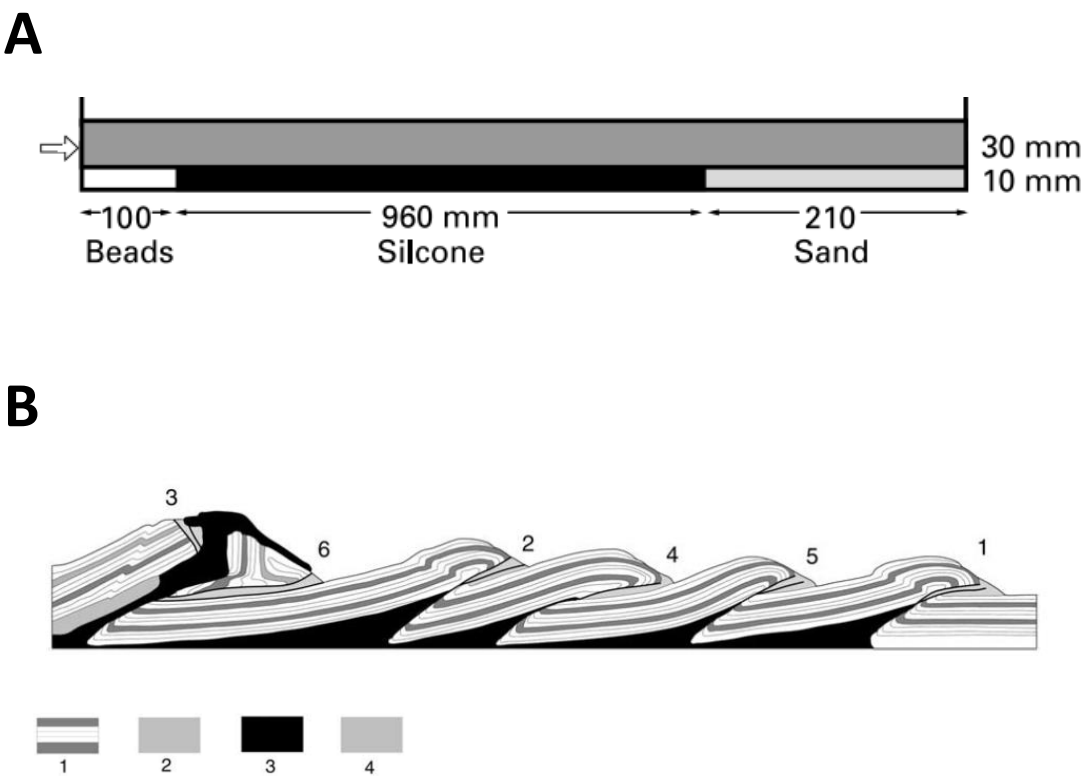

Figure 3.11: (A) Line drawing illustrating the initial cross-sectional geometry of Model 4 in Costa and Vendeville (2002). (B) Line drawing of a vertical cross-section cut in Model 4 (Costa and Vendeville, 2002). Symbols: (1) brittle sand cover; (2) glass microbeads; (3) silicone polymer (weak, viscous décollement); (4) slumped sand.

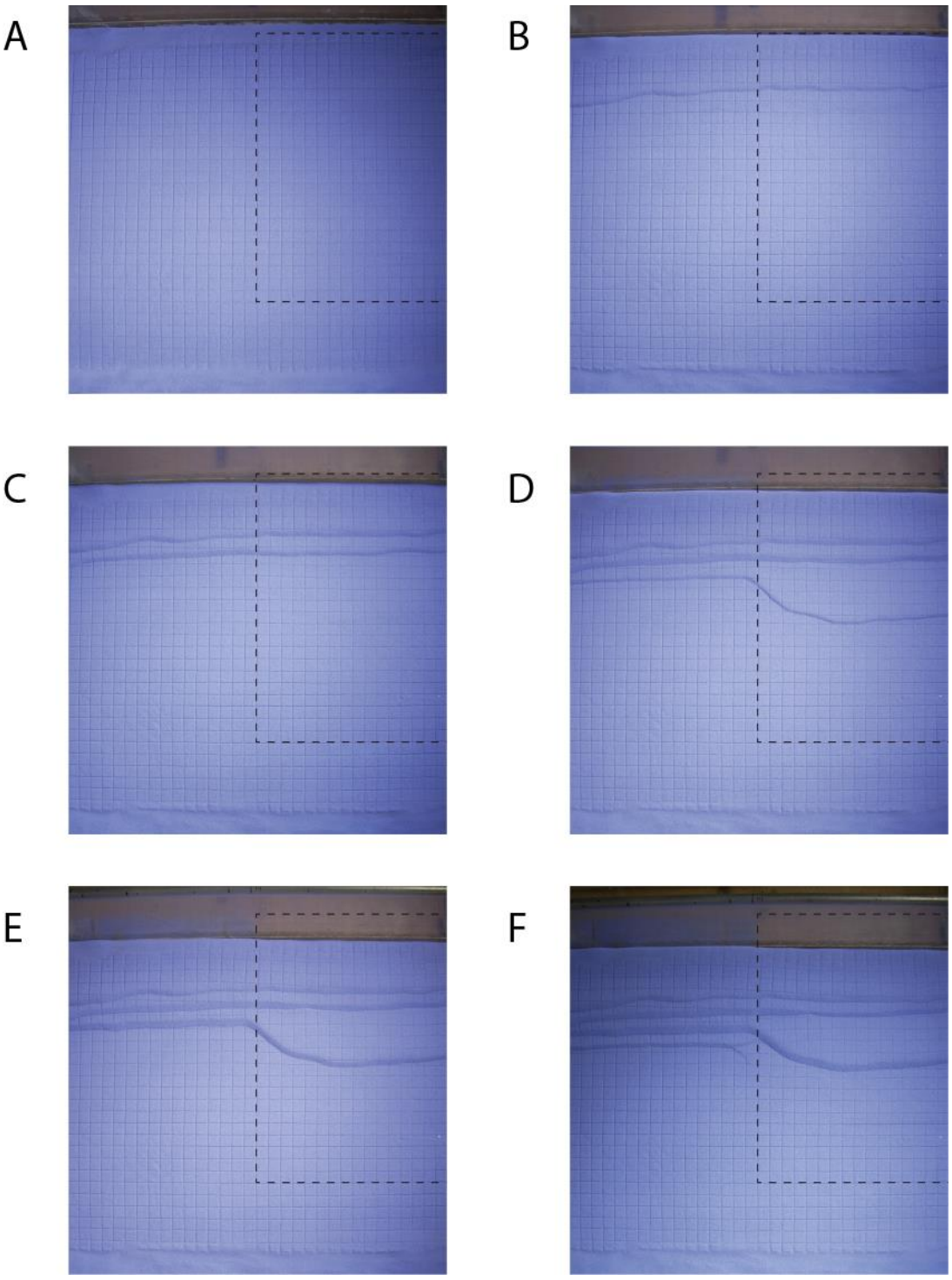

Figure 3.12: Series of selected top view images of Model 4 at incremental shortening of (A) 0 cm, (B) 1 cm, (C) 2 cm, (D) 3 cm, (E) 4 cm, (F) 5 cm, (G) 6 cm, (H) 7 cm, (I) 8 cm, (J) 9 cm, (K) 10 cm and (L) 11 cm. The boundary of the silicone gel is indicated by the black dashed line.

G

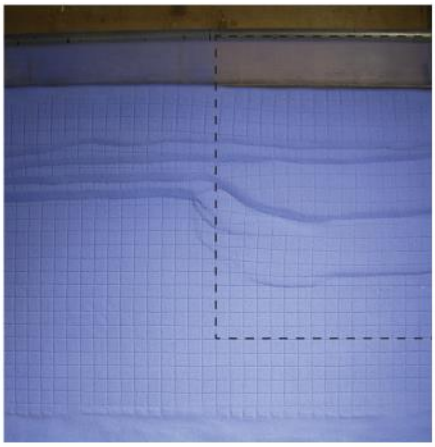

H

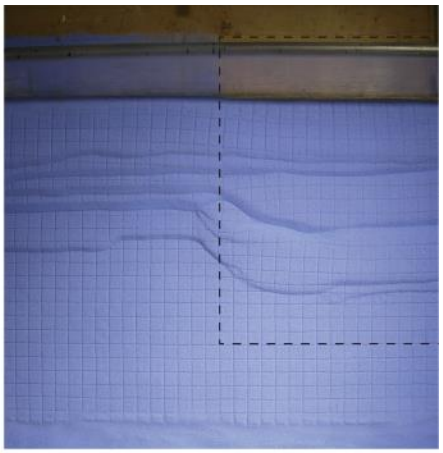

I

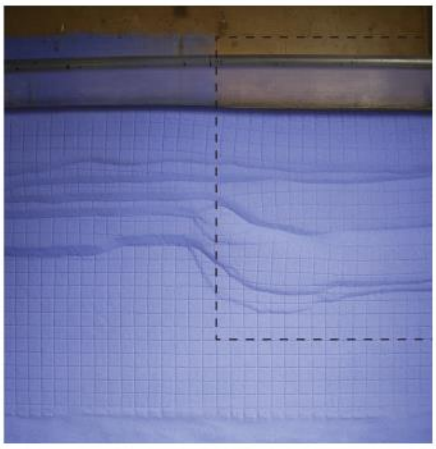

J

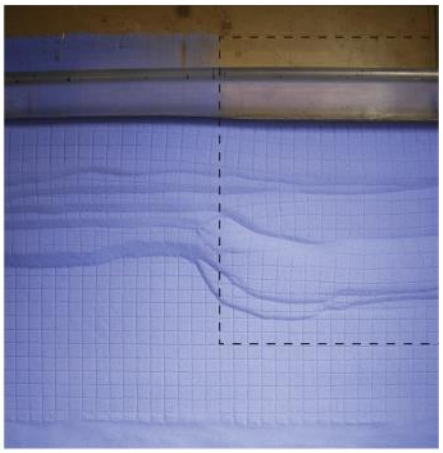

K

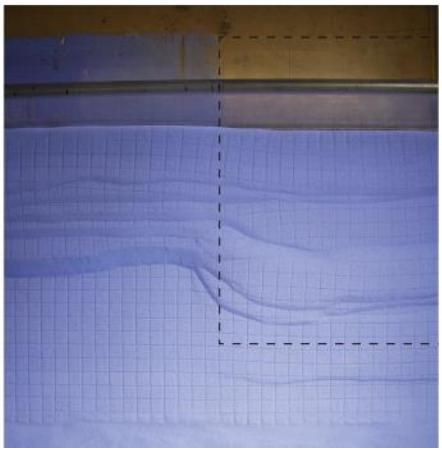

L

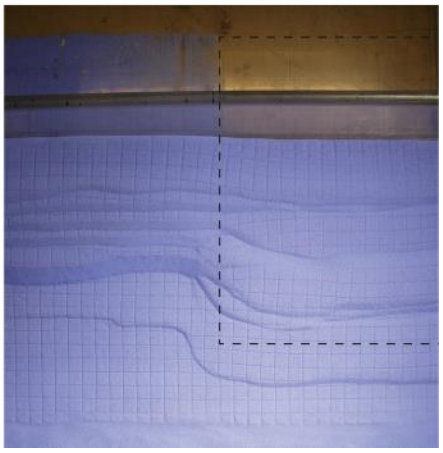

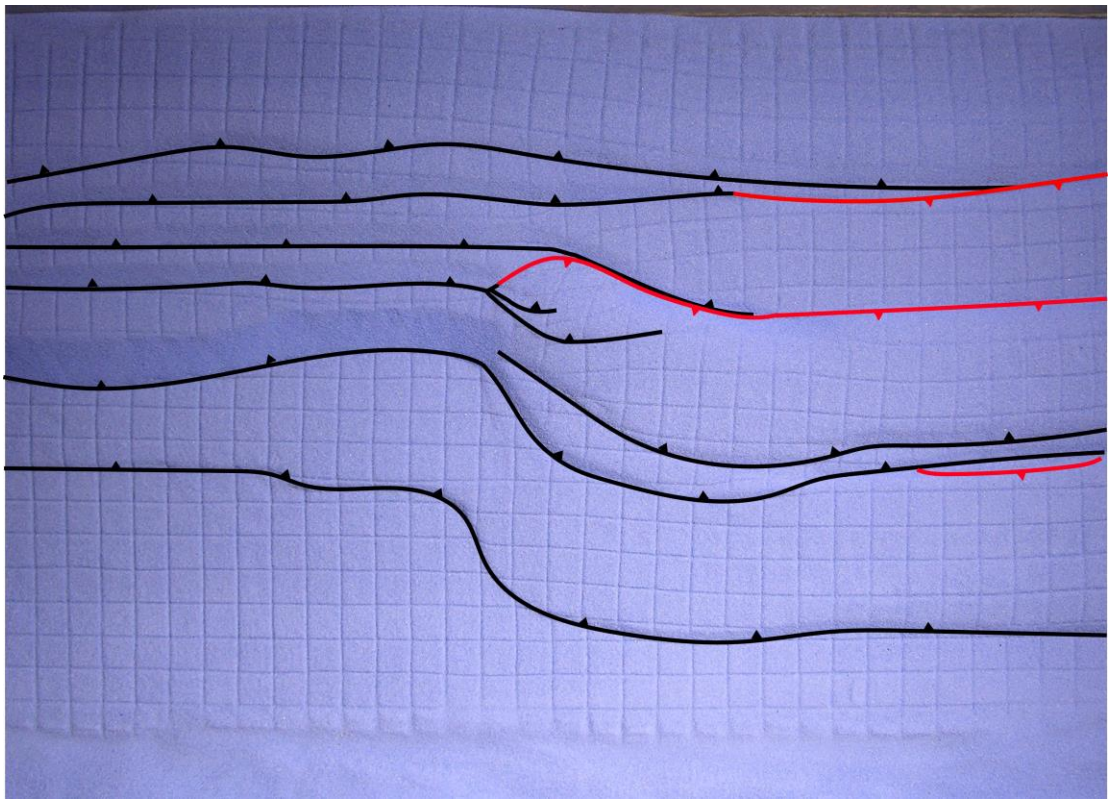

Figure 3.13: The top view image of the final stage of Model 4. Forethrusts are traced using black lines with teeth on hanging wall. Backthrusts are traced using red lines with teeth on hanging wall.

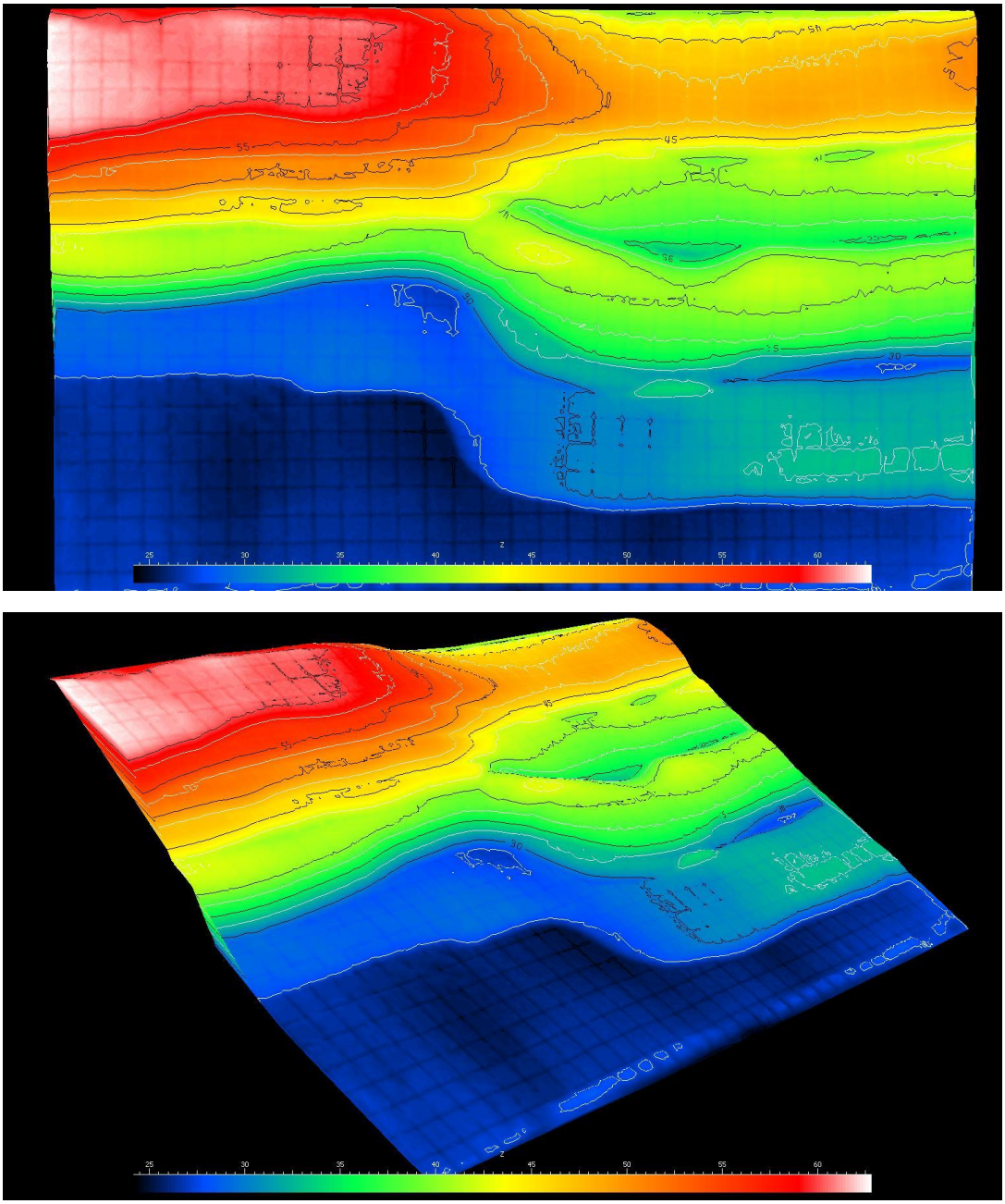

Figure 3.14: 3D scanner images of the final stage of Model 4 showing the elevation from two angles. Unit in the color bar is mm.

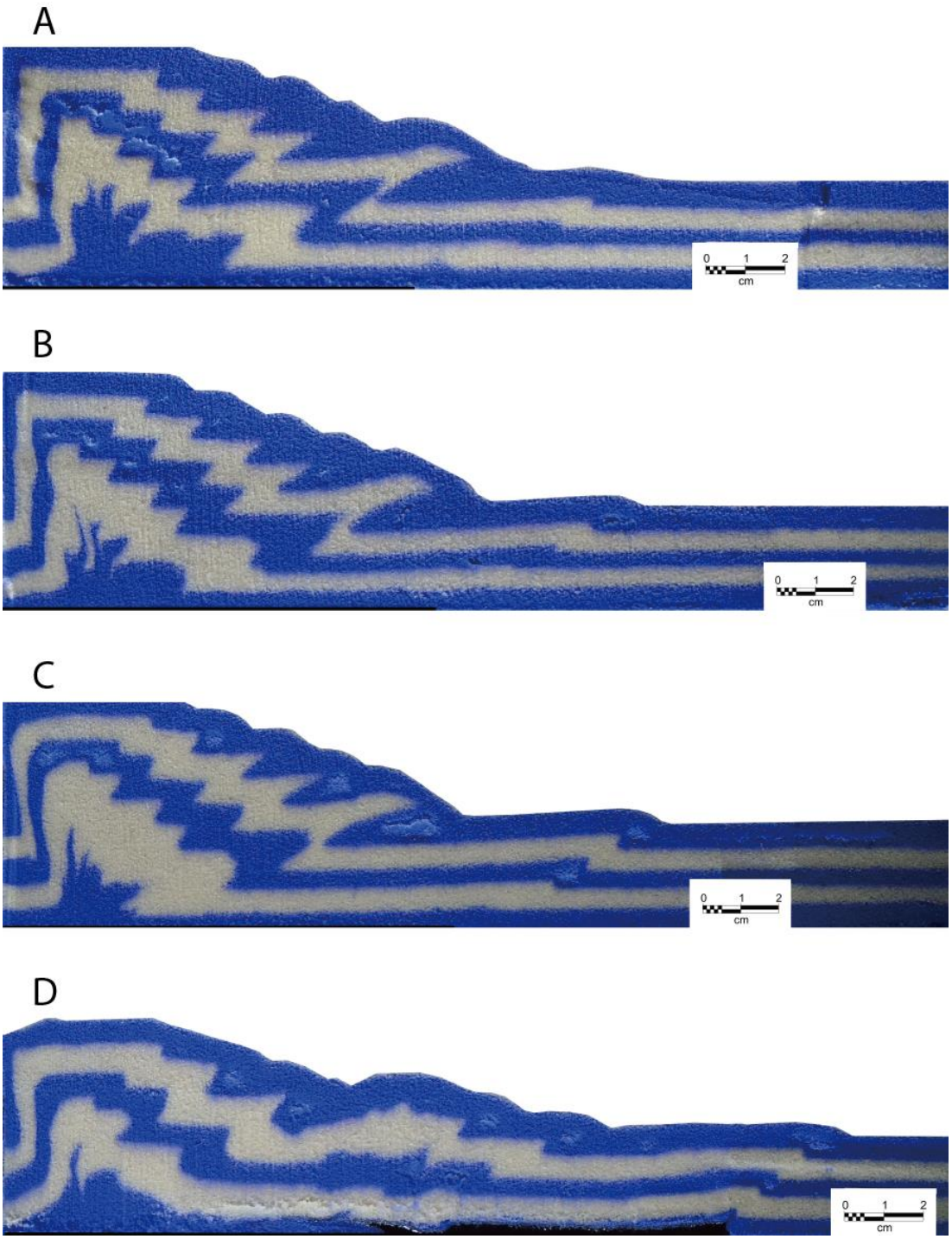

Figure 3.15: Series of cross-sectional images of Model 4. The location of each cross-section is labeled on the final stage top view image at the end.

E

F

G

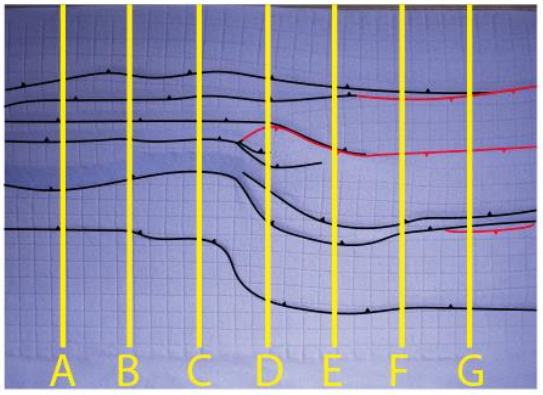

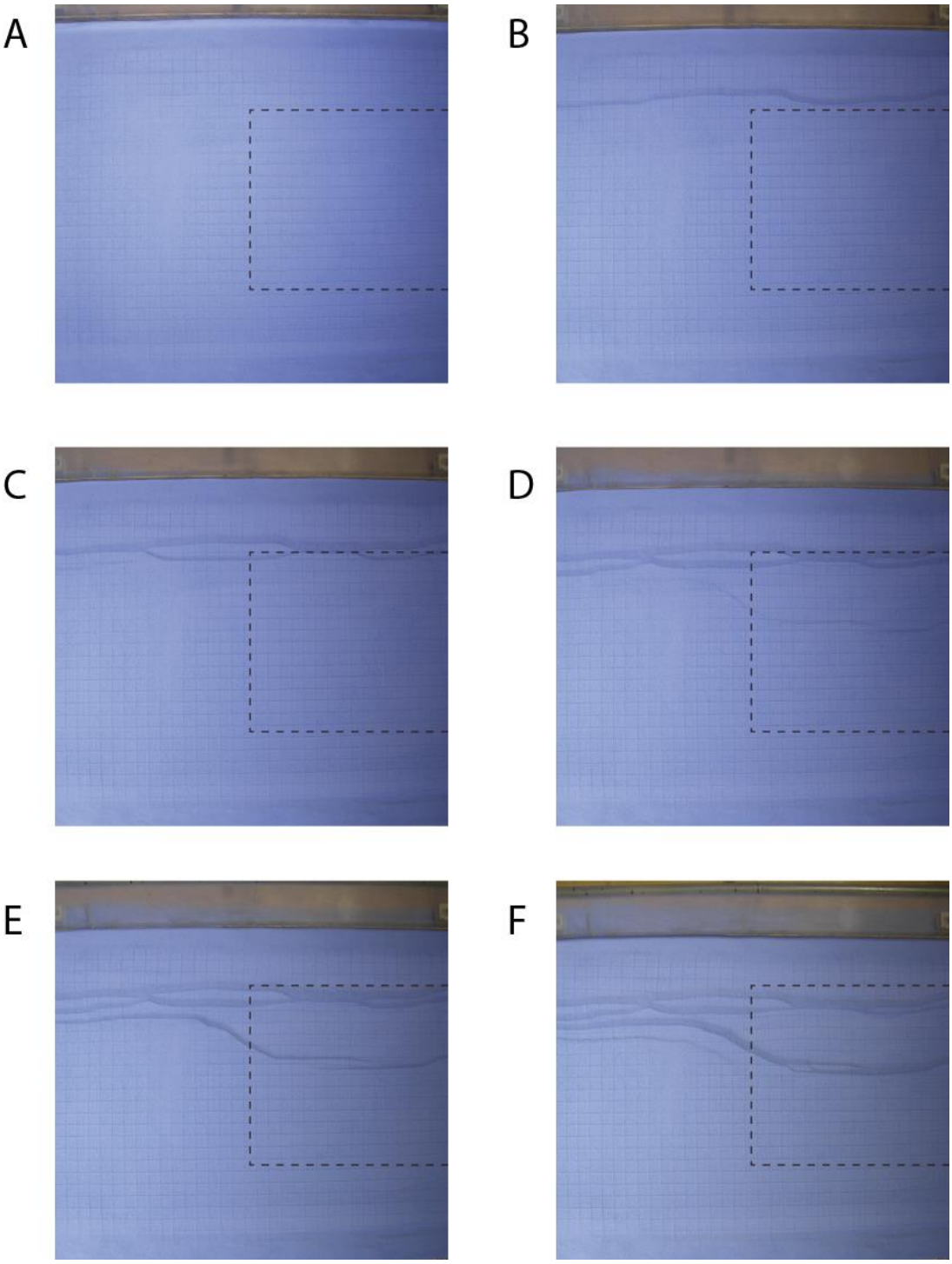

Figure 3.16: Series of selected top view images of Model 5 at incremental shortening of (A) 0 cm, (B) 1 cm, (C) 2 cm, (D) 3 cm, (E) 4 cm, (F) 5 cm, (G) 6 cm, (H) 7 cm and (I) 8 cm. The boundary of the silicone gel is indicated by the black dashed line.

G

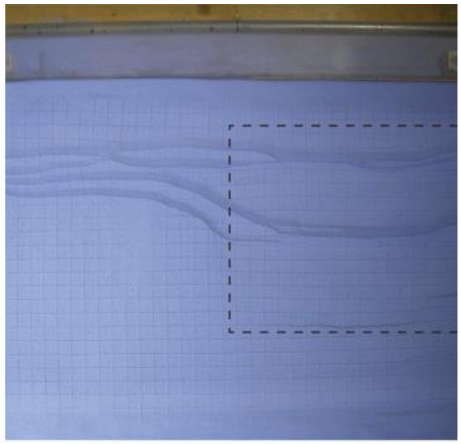

H

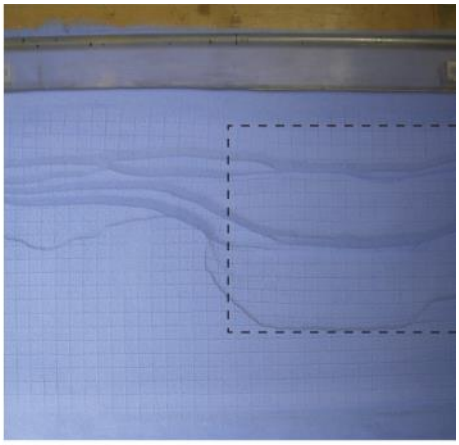

I

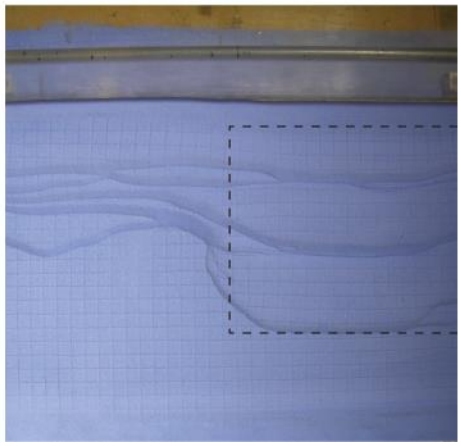

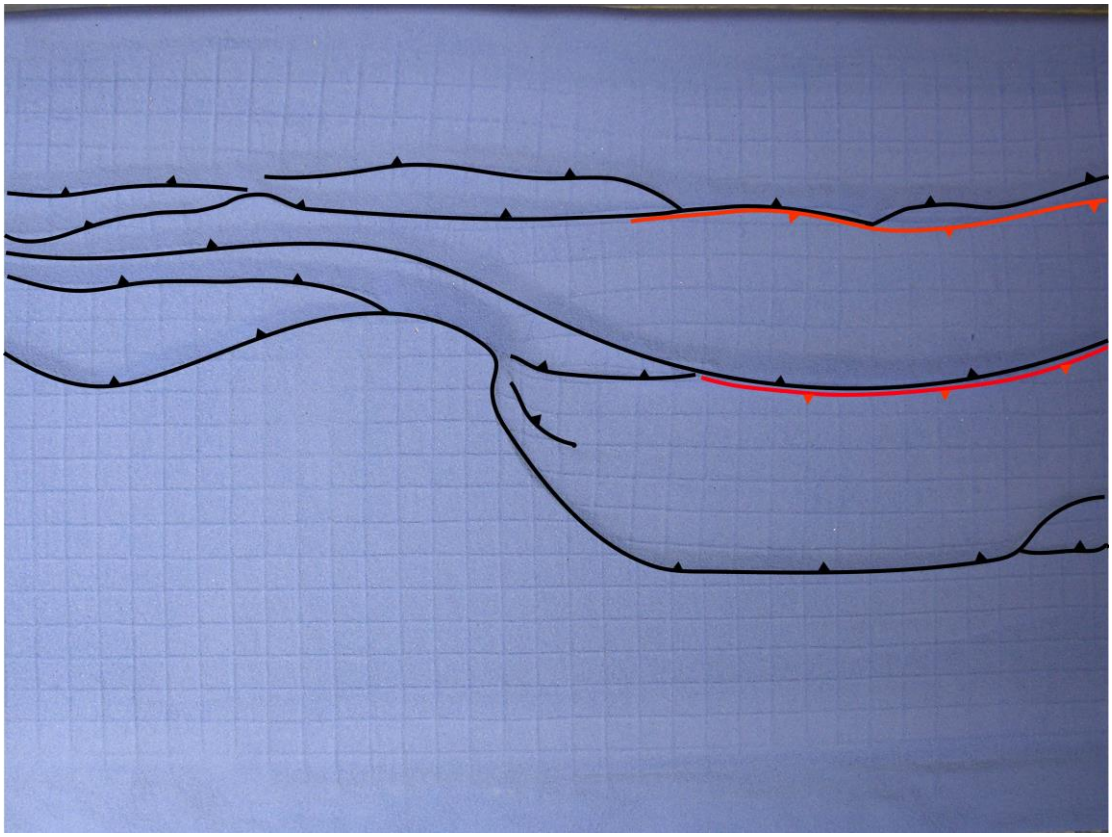

Figure 3.17: The top view image of the final stage of Model 5. Forethrusts are traced using black lines with teeth on hanging wall. Backthrusts are traced using red lines with teeth on hanging wall.

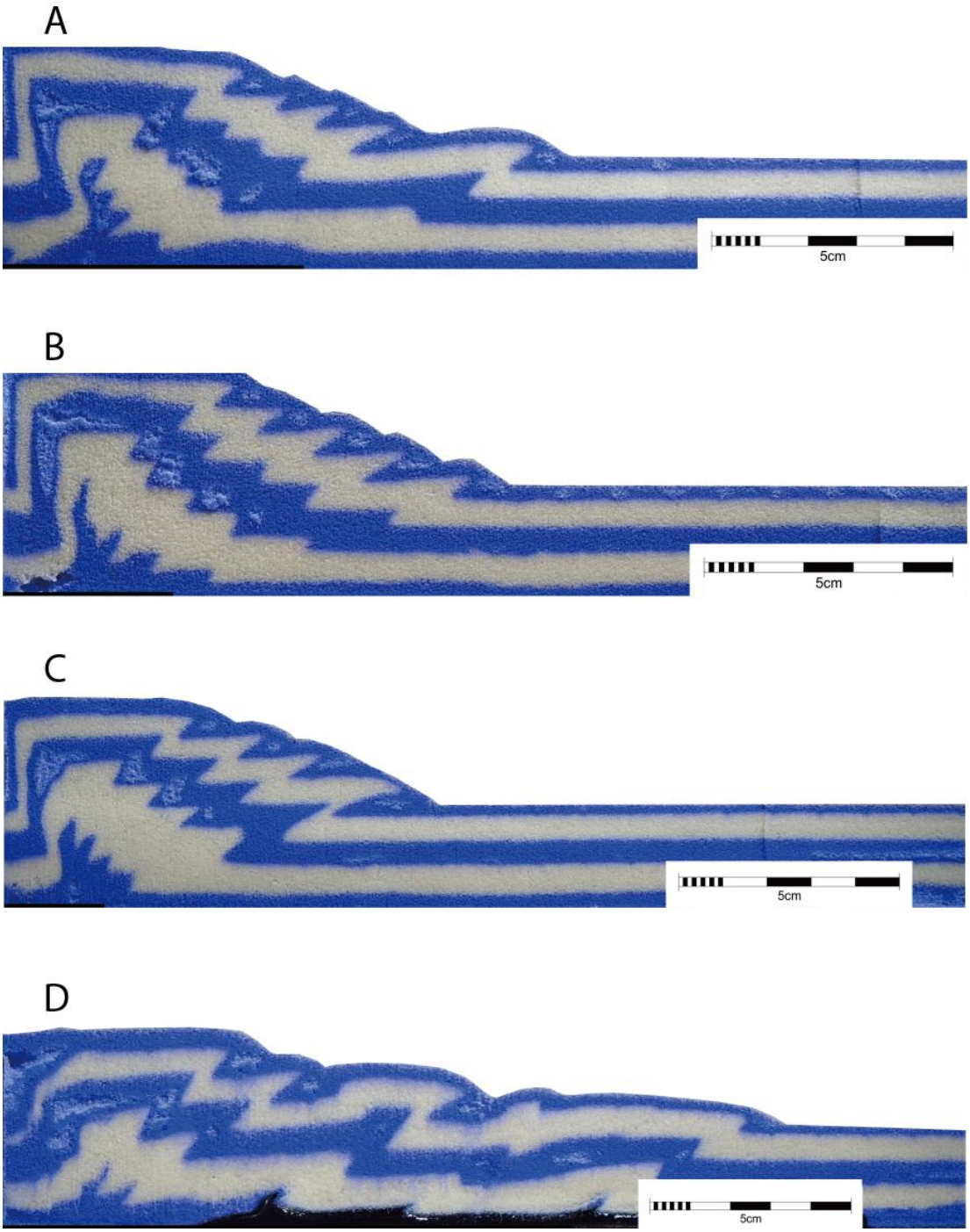

Figure 3.18: Series of cross-sectional images of Model 5. The location of each cross-section is labeled on the final stage top view image at the end.

E

F

G

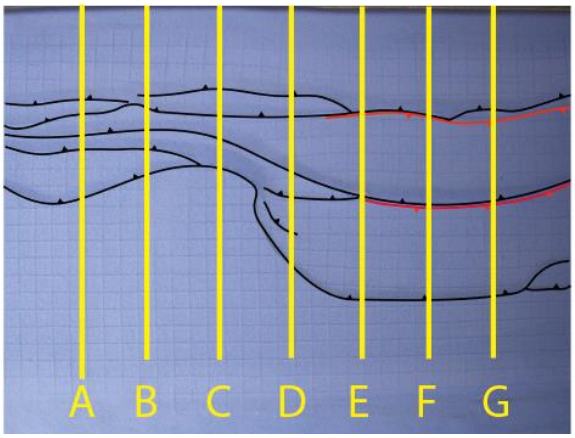

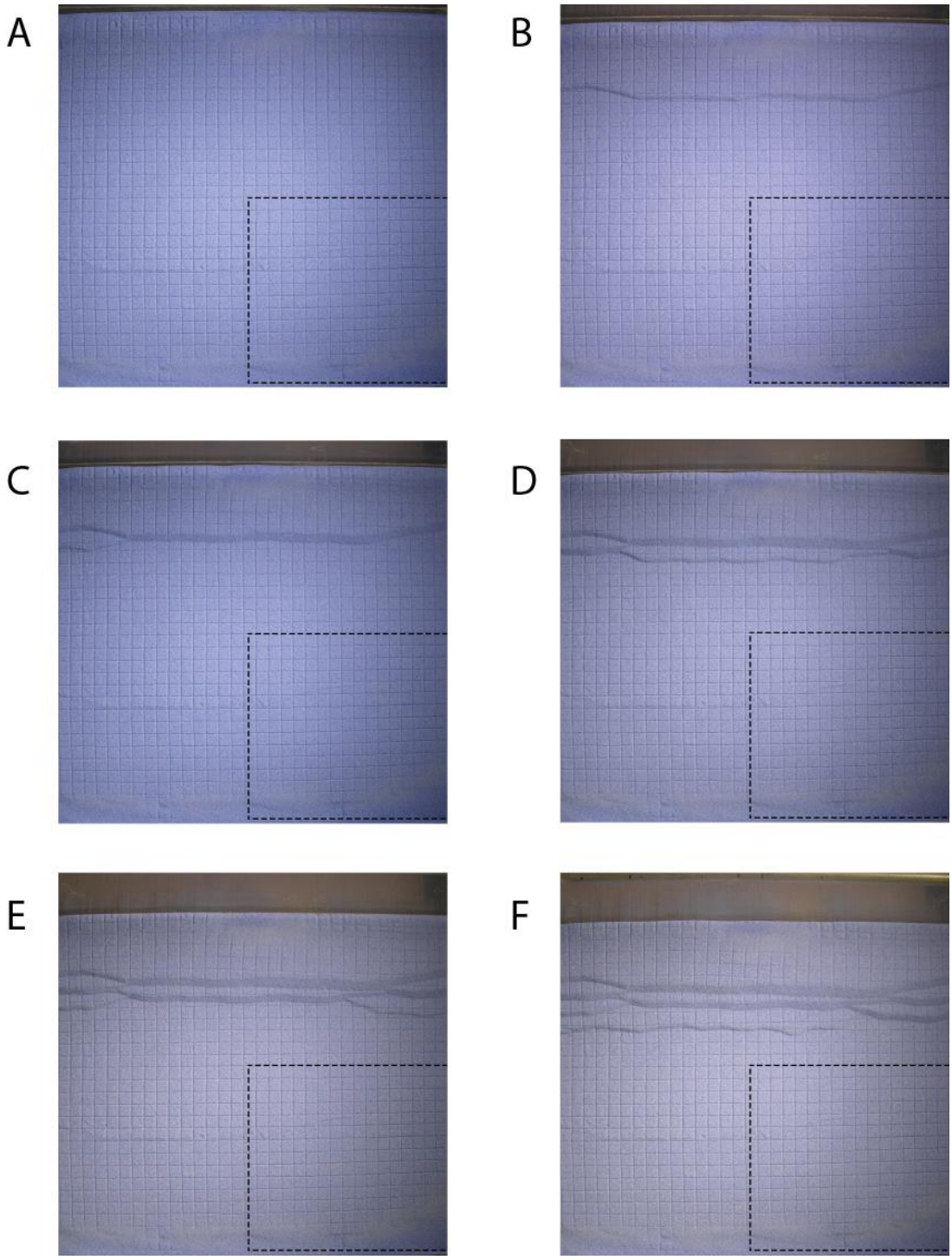

Figure 3.19: Series of selected top view images of Model 6 at incremental shortening of (A) 0 cm, (B) 1 cm, (C) 2 cm, (D) 3 cm, (E) 4 cm, (F) 5 cm, (G) 6 cm, (H) 7 cm, (I) 8 cm, (J) 9 cm, (K) 10 cm, (L) 11 cm, (M) 12 cm and (N) 13 cm. The boundary of the silicone gel is indicated by the black dashed line.

G

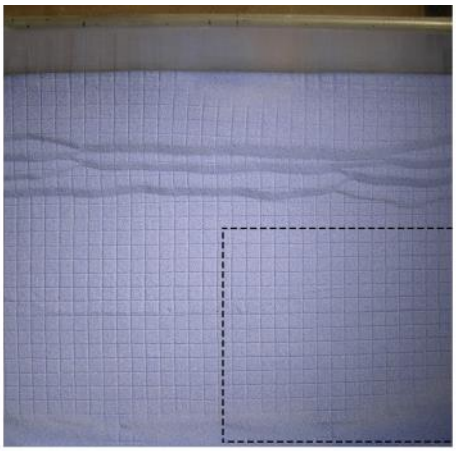

H

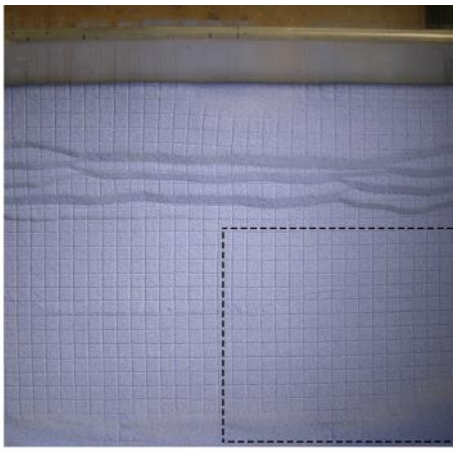

I

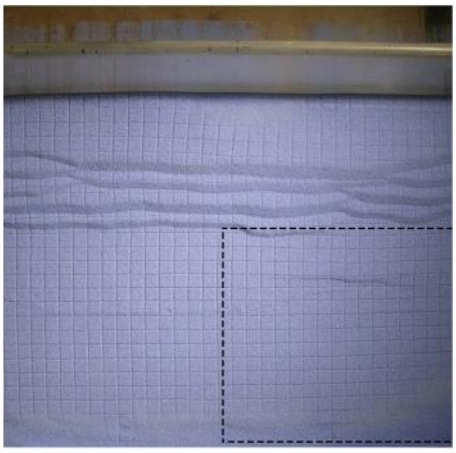

J

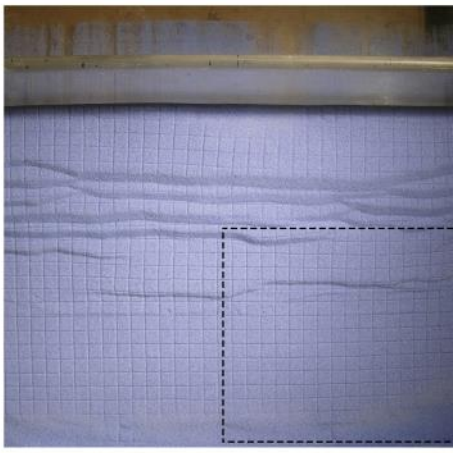

K

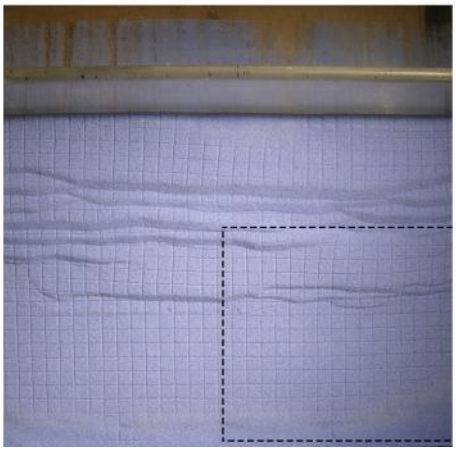

L

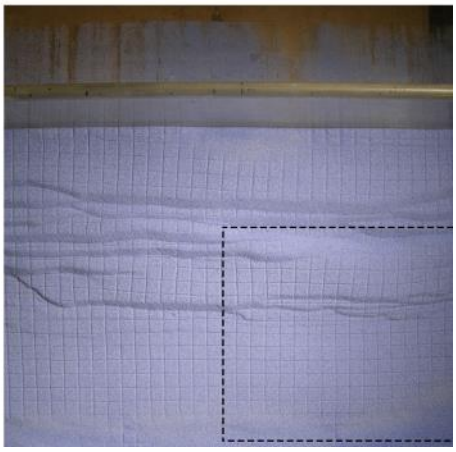

M

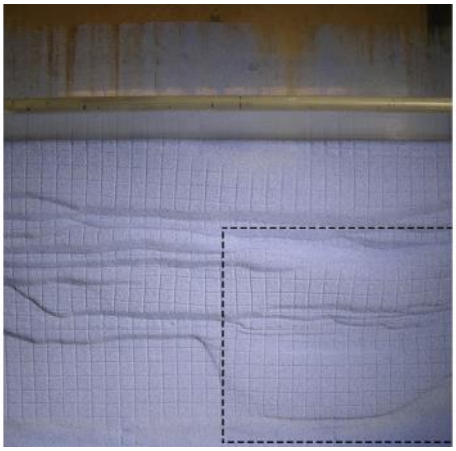

N

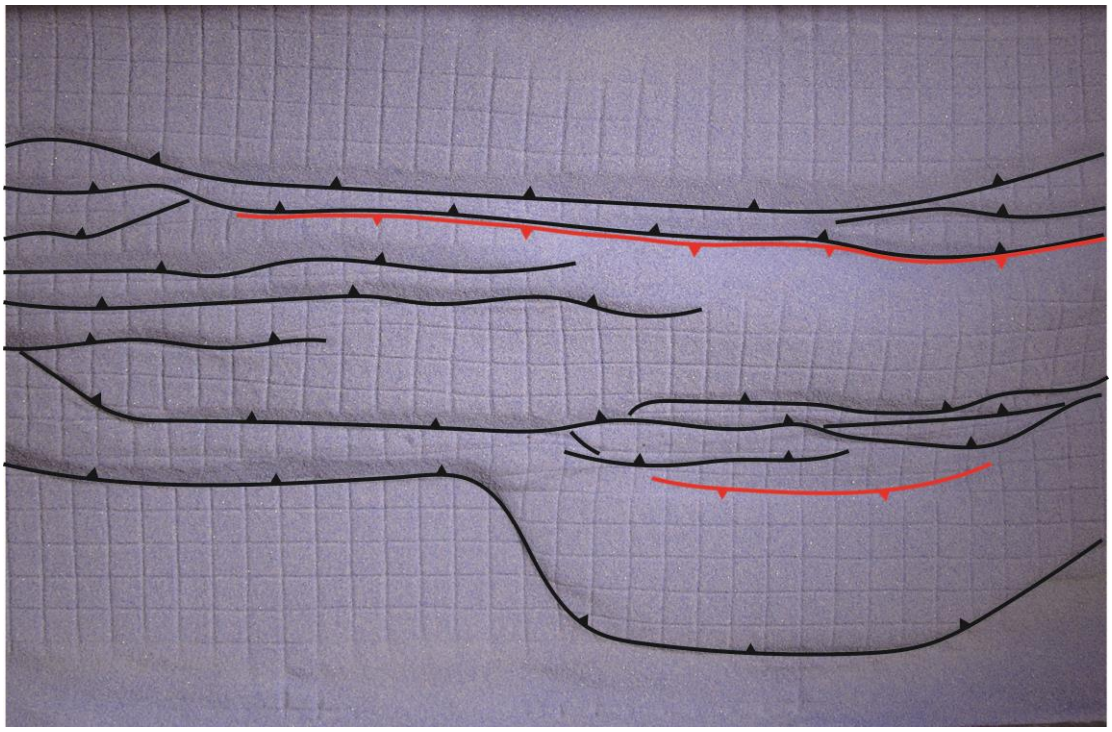

Figure 3.20: The top view image of the final stage of Model 6. Forethrusts are traced using black lines with teeth on hanging wall. Backthrusts are traced using red lines with teeth on hanging wall.

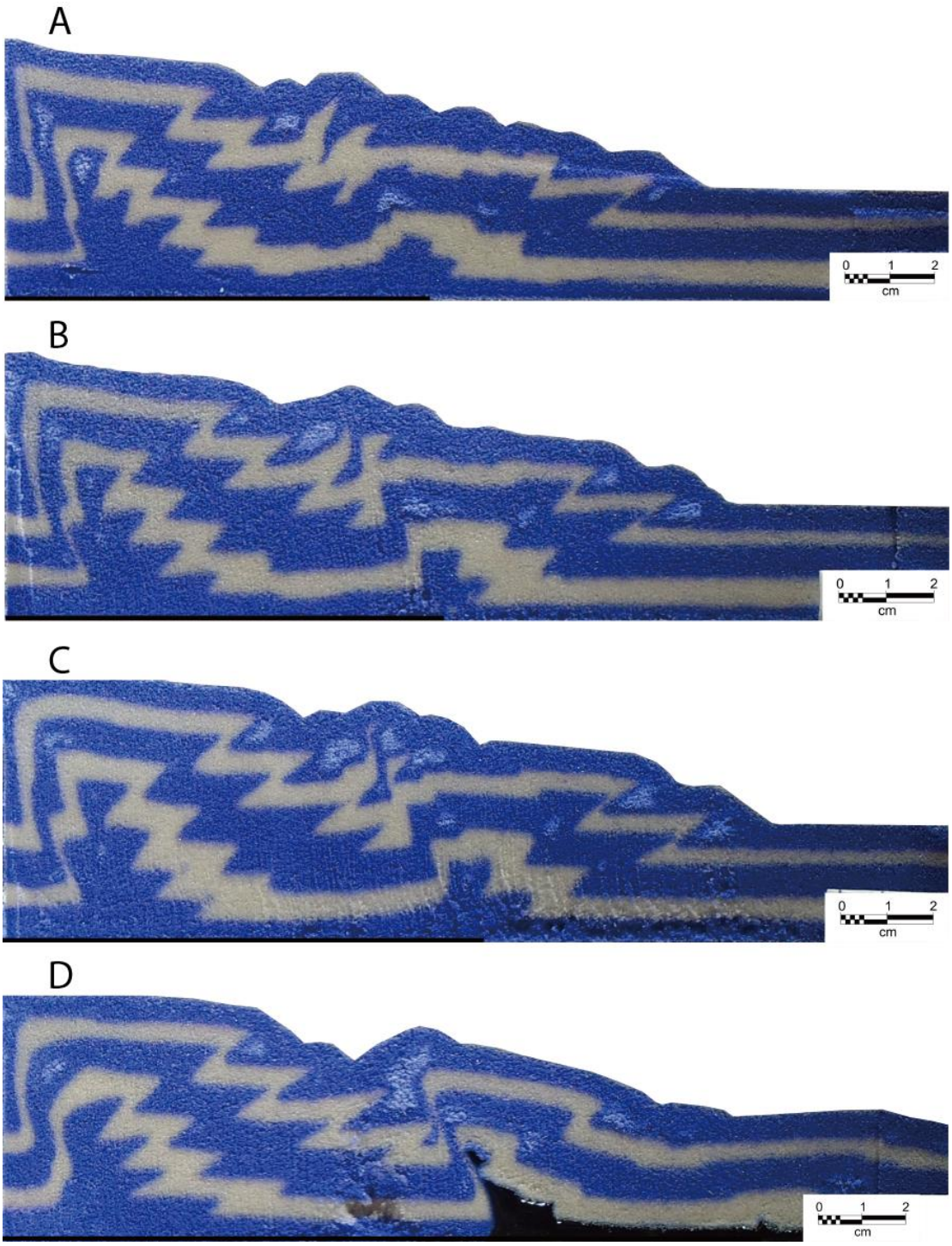

Figure 3.21: Series of cross-sectional images of Model 6. The location of each cross-section is labeled on the final stage top view image at the end.


E
0 1 2
cm


F
0 1 2
cm


G
0 1 2
cm

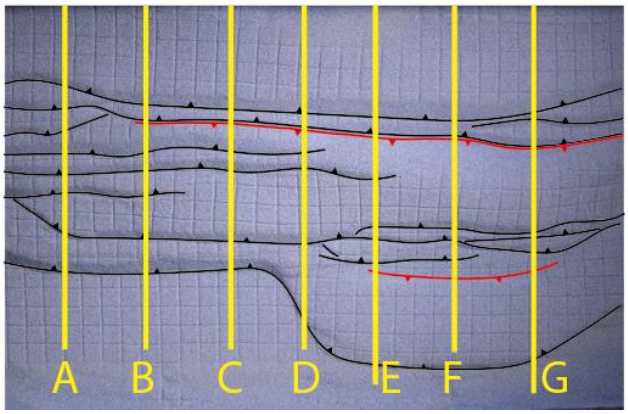
A
B
C
D
E
F
G

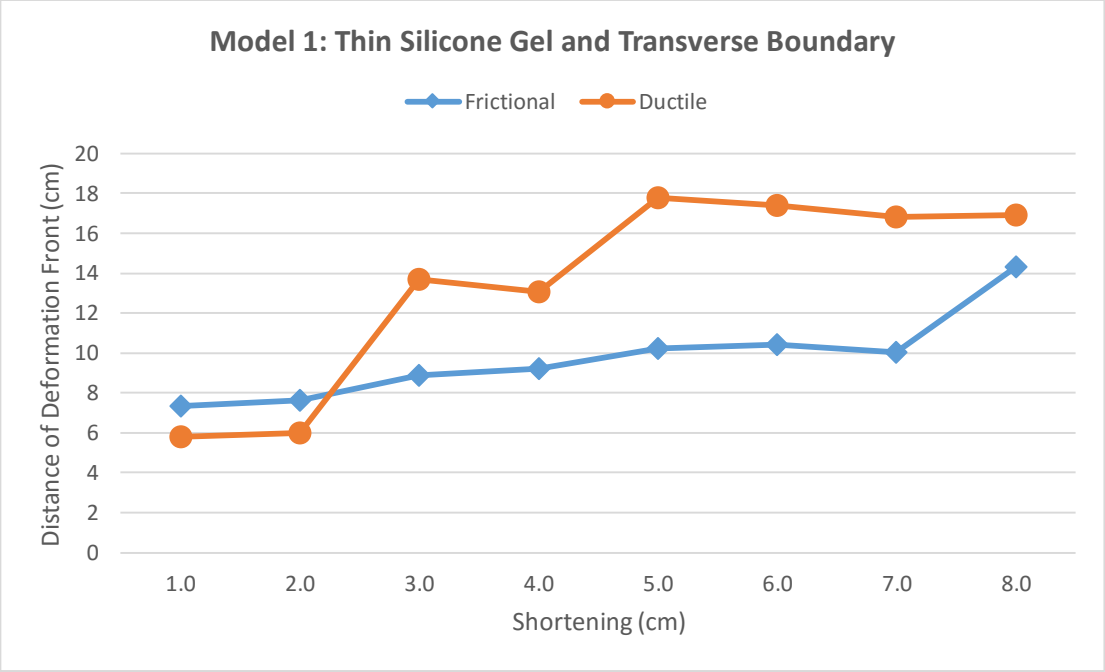

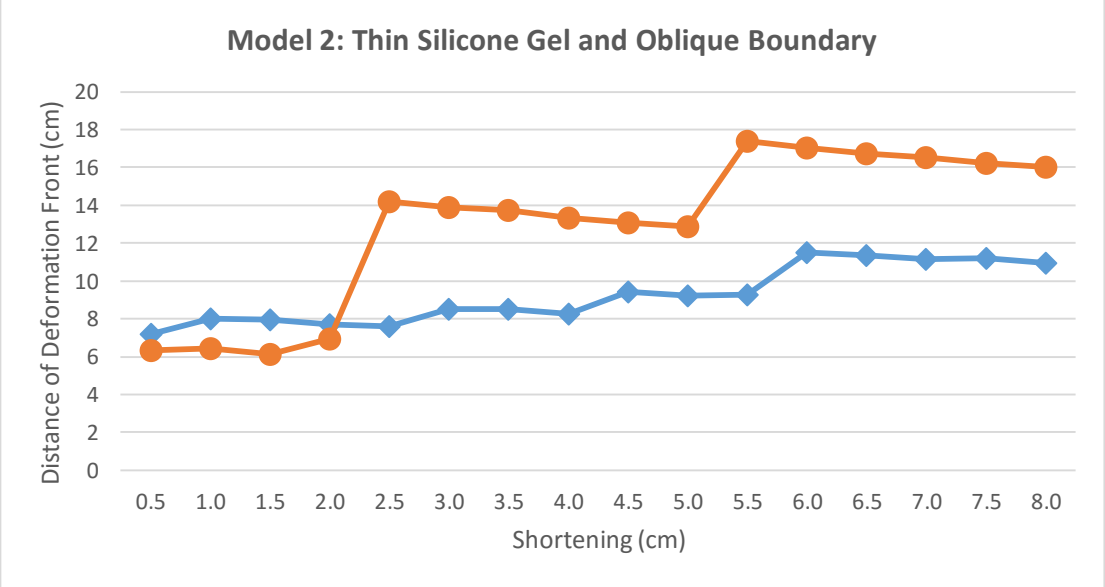

Figure 3.22: Graphical plot displaying the distance of the deformation front with respect to the movable plate versus a cumulative shortening distance. The plots further confirmed that the deformation developed above the ductile detachment (orange circle lines) propagated farther and faster than the deformation above the frictional detachment (blue diamond lines).

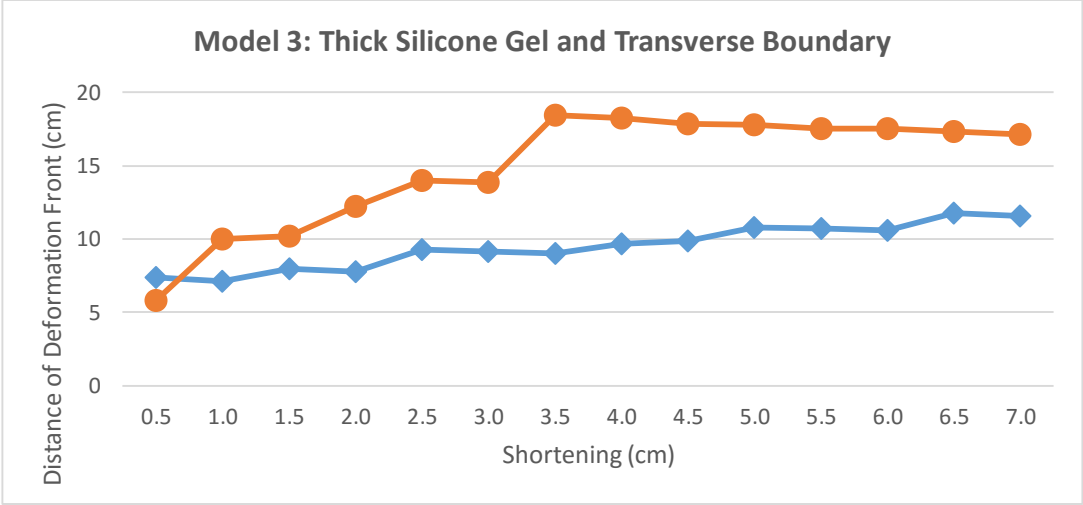
Model 3: Thick Silicone Gel and Transverse Boundary
Distance of Deformation Front (cm)
0
5
10
15
20
0.5
1.0
1.5
2.0
2.5
3.0
3.5
4.0
4.5
5.0
5.5
6.0
6.5
7.0
Shortening (cm)

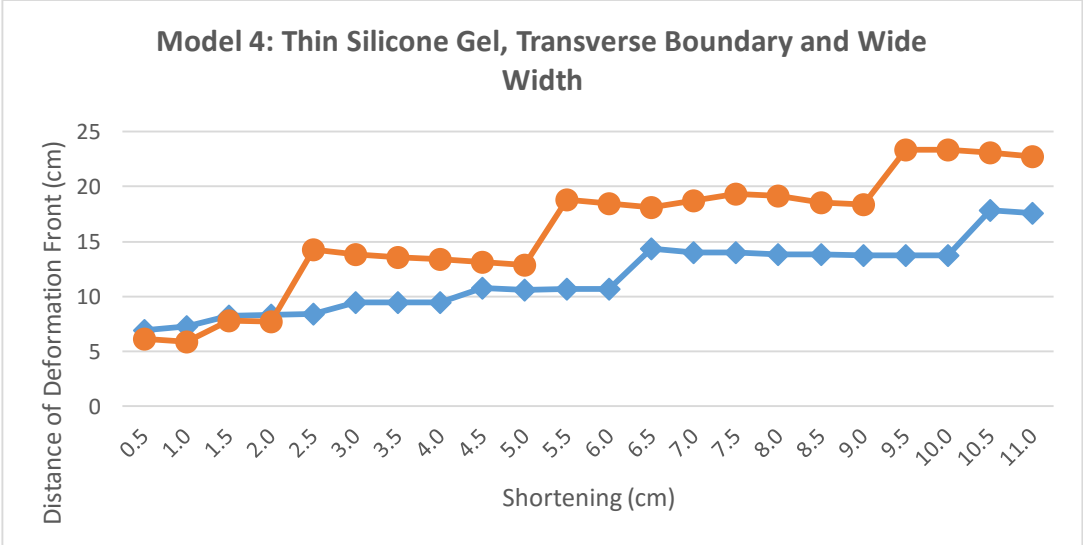
Model 4: Thin Silicone Gel, Transverse Boundary and Wide Width
Distance of Deformation Front (cm)
0
5
10
15
20
25
0.5
1.0
1.5
2.0
2.5
3.0
3.5
4.0
4.5
5.0
5.5
6.0
6.5
7.0
7.5
8.0
8.5
9.0
9.5
10.0
10.5
11.0
Shortening (cm)

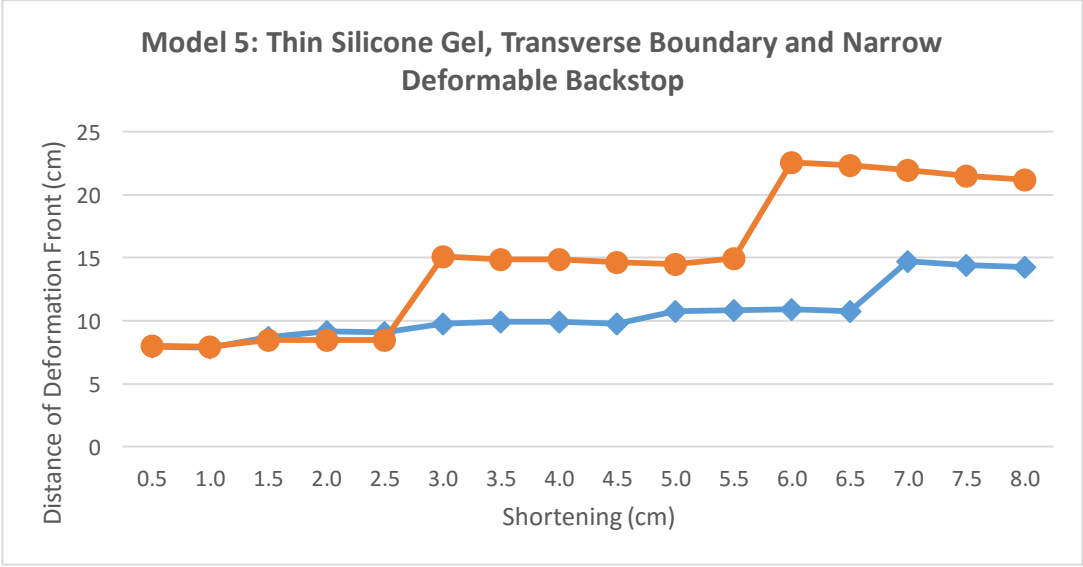
Model 5: Thin Silicone Gel, Transverse Boundary and Narrow Deformable Backstop
Distance of Deformation Front (cm)
0
5
10
15
20
25
0.5
1.0
1.5
2.0
2.5
3.0
3.5
4.0
4.5
5.0
5.5
6.0
6.5
7.0
7.5
8.0
Shortening (cm)

CHAPTER 4: DISCUSSION

4.1. *Taper Analysis*

Previous work on Coulomb taper theory (Davis et al., 1983; Davis and Engelder, 1985) suggested that a decrease in basal friction μ_b decreases the critical taper ($\alpha + \beta$). In this study, frictional and ductile basal detachments were combined within a single model. There was no surface slope or basement dip in the initial setting so the taper developed as a result of the deformation. Lateral comparison between the cross-sections from either detachment domain was used to study the variations in taper geometry. As expected, the taper developed above the frictional detachment was steeper and narrower than the taper developed above the ductile detachment (Table 3). Some additional observations relating to the geometry of the taper were made in the study. These are related to the lateral propagation of the structures, the steeper wedge created by the deformable backstop, and the frontal pinch-out of the ductile detachment layer.

Table 3: Measurements of taper angles for six models.

	Model 1	Model 2	Model 3	Model 4	Model 5	Model 6
Frictional Detachment	14.9°	24.2°	20.4°	15.3°	21.4°	12.9°
Ductile Detachment	5.4°	6.4°	2.8°	5.8°	2.9°	7.3°

Because of the lateral variation from a frictional to a ductile detachment, the taper geometry was modified by the influence of the deformation along trend, in particular, the lateral propagation of faults. In a number of experiments, the location of the frontal fault above the frictional detachment was influenced by the position of

the frontal thrust above the ductile detachment, thereby reducing the taper angle in the frictional domain. Thereofore, it is unlikely that a critical taper developed in the frontal part of the belt developed before the formation of the frontal thrust. Also in Model 6, a backthrust within the ductile domain propagated laterally into the frictional domain. This also modified the taper geometry in the frictional domain. These factors are expected to influence the taper geometry in natural fold-thrust belts.

The presence of the wide backstop in Models 6 resulted in a steep taper behind the detachment fold belt, and this increased the taper angle of the detachment fold belt in front of it. Therefore, the taper geometry of detachment fold belts in front of major thrust belts was likely modified by the presence of the thrust belt.

Finally, the frontal pinch-out of the ductile layer controls the location of the frontal structure, and therefore of the taper width. A comparison of the 3D surface models for Models 3 and 4 shows that a wide detachment layer also results in a wide fold belt and therefore a smaller taper angle than a narrower detachment layer in the ductile detachment domain. Furthermore, this also results in a narrower taper angle in the frictional detachment domain.

4.2. ***Natural Cases***

Models with different configurations of the silicone layer setup confirmed that the width of the ductile layer constrained the extent of the overlying structures. The oblique lateral boundary of the ductile layer (Model 2) resulted in an oblique deformation front at the transfer zone between the frictional and ductile detachments while a transverse lateral boundary of the ductile layer (Model 1) resulted in a thrust

front with a high angle to the transport direction. The relationship can be applied to natural cases like the Salt Range and Potwar Plateau and the Kuqa fold-thrust belt.

Figure 4.1 is a structural map showing the main structural elements of the Salt Range and Potwar Plateau. The Salt Range and Potwar Plateau is a thin-skinned fold-thrust belt underlain by thick Lower Cambrian Evaporites of the Salt Range Formation (Backer, 1987; Butler et al., 1987; Burbank and Beck, 1989). The dashed line representing the limit of the salt basin delimits the boundary of the structures of the Salt Range and Potwar Plateau. The transverse boundary setup of the silicone layer (Model1) simulates the NNW-SSE trending deformation front at the west of the Salt Range which is related to the western termination of the Salt Range Formation evaporites. The differential propagation rates on either side of the western boundary of the salt basin are also consistent with the experimental results. The geometry of the entire area is best simulated by Model 6, with a frictional thrust located behind the fold belt with the salt detachment as well as lateral to it.

The Kuqa basin is located at the southern piedmont of the southern Tian Shan at 80.5°–84°E longitude. It is about 400 km long from east to west with a width of 30–70 km (Jia, 1997), and typically contains three to four linear of fold-and-thrust zones. These folds are underlain by thick accumulations of salt which locally exceeds 3000 m (Li et al., 2012). From the map view of the Kuqa basin (Figure 4.2), it is clear that the extent of the structures is limited by the edge of the Paleocene-Eocene Kumugeliemu salt (the blue dashed line). Beyond the SW boundary of the salt, there are only a few thrusts or anticlines. The deformation front beyond the salt boundary is far behind the deformation front developed above the salt. Furthermore, at the SW

edge of the Kuqa basin, structures are along the NW-SE trend which is oblique to the typical strike of the structure in the basin. Similar to the cause of the oblique deformation front at the transfer zone in Model 2, these oblique structures are related to the oblique lateral boundary of the salt layer. Again the overall geometry is best simulated by the complex frictional–ductile system of Model 6, but with an oblique salt boundary (Model 2).

In addition to the map view analysis of the Kuqa basin, the cross-section of Line-A is shown in Figure 4.3. The section Line-A shares some similar structural styles with the cross-section in the ductile detachment domain of Model 6 (Figure 3.21E). A salt cored wedge was developed in front of the wedge built with deformable backstop, in this case, the Tian Shan Mountain (Figure 4.2). Similar to the symmetrical box fold developed near the frontal boundary of the silicone layer, two symmetrical salt cored anticlines developed close to the frontal pinch-out of the salt layer.

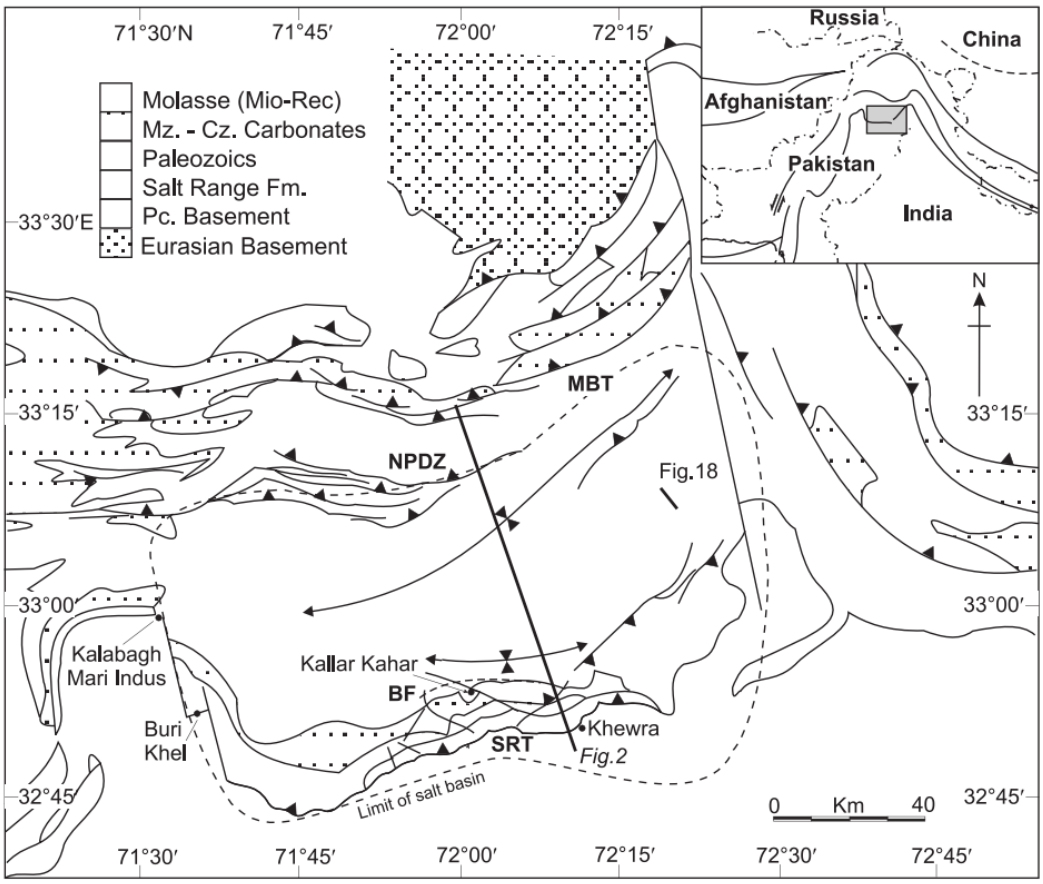

Figure 4.1: Major structural elements of Salt Range and Potwar Plateau (Cotton and Koyi, 2000; modified from Treloar et al., 1992). NPDZ—Northern Potwar deformation zone; MBT—Main Boundary thrust; SRT—Salt Range thrust; and BF—Basement fault.

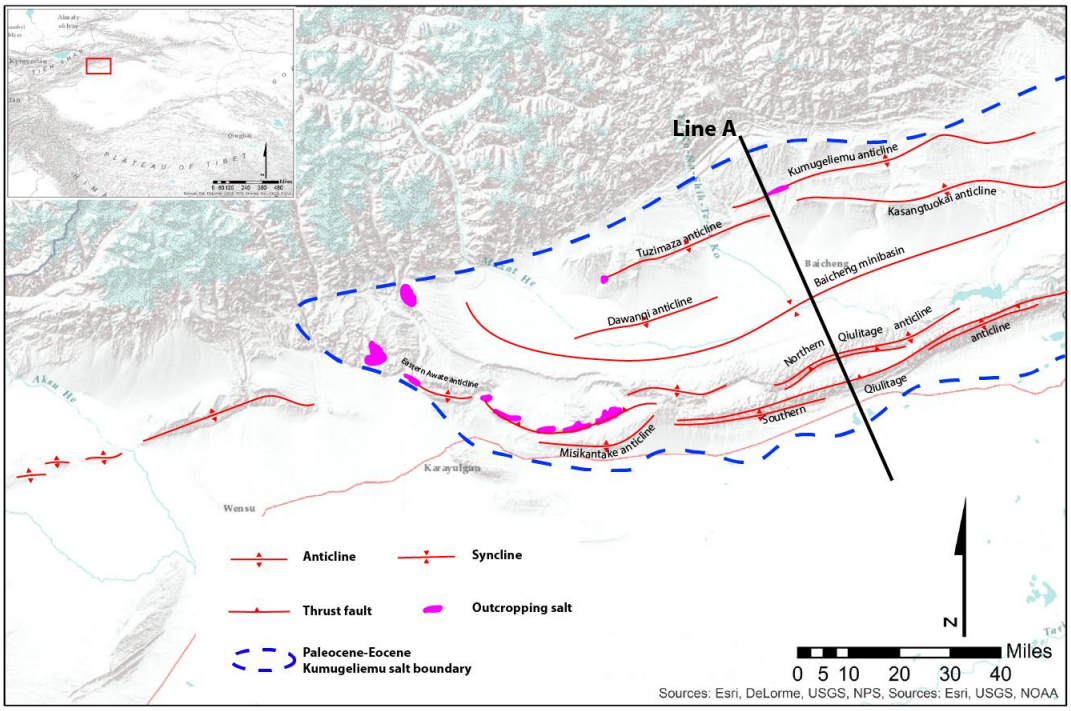

Figure 4.2: Topographic map of the Kuqa basin showing major structural elements (modified from Li et al., 2012).

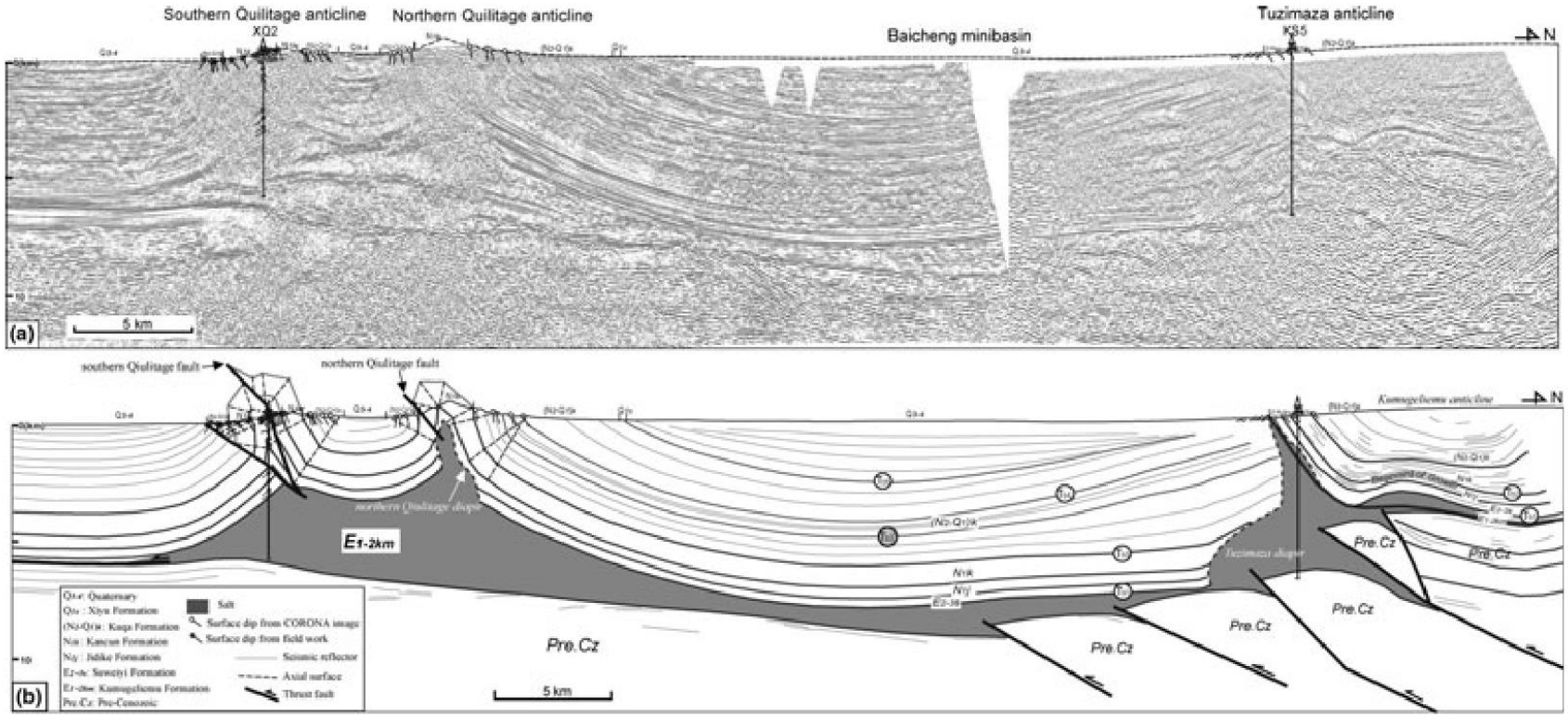

Figure 4.3: (a) Uninterpreted depth seismic section Line-A (location in Figure 4.2), and (b) interpreted section Line A line drawing showing salt structures of the middle part of the Kuqa basin (Li et al., 2012).

CHAPTER 5: SUMMARY

The observations and analyses of the sandbox analogue models of structures above ductile and frictional detachments lead to the following summary.

1. The deformation front above the ductile detachment propagated farther and at a higher rate than that above the frictional detachment resulting in a narrower taper of the ductile detachment domain.
2. A ductile detachment resulted in detachment folds with both forethrusts and backthrusts whereas a frictional detachment resulted in thrust fault systems (duplexes) with only forethrusts.
3. Larger thickness ratios between the ductile layer and overburden layers resulted in more asymmetric folds and a higher propagation rate than smaller thickness ratios.
4. The width of the ductile detachment controlled the width of the detachment fold belt, so that a wider ductile detachment resulted in a narrower taper.
5. The geometry of the detachment boundary strongly controlled the geometry of the boundary of the overlying structures. An oblique boundary of the ductile detachment resulted in an oblique deformation front in the transition zone between the two settings.
6. The structures developed above the frictional detachment was affected by the propagation of adjacent structures developed above the ductile detachment. The thrust spacing above the frictional detachment increased at late stages minimizing the lag between the two deformation fronts.

7. A wide deformable backstop was deformed into an imbricate wedge that formed behind the detachment fold belt in the ductile detachment domain.

REFERENCES

Bahroudi, A., & Koyi, H. (2003). Effect of spatial distribution of Hormuz salt on deformation style in the Zagros fold and thrust belt: an analogue modelling approach. *Journal of the Geological Society, 160*(5), 719-733.

Baker, D. M. (1987). *Balanced structural cross-sections of the central Salt Range and Potwar Plateau of Pakistan: shortening and overthrust deformation*.

Bose, S., Mandal, N., Mukhopadhyay, D. K., & Mishra, P. (2009). An unstable kinematic state of the Himalayan tectonic wedge: Evidence from experimental thrust-spacing patterns. *Journal of Structural Geology, 31*(1), 83-91.

Burbank, D. W., & Beck, R. A. (1989). Early Pliocene uplift of the Salt Range; temporal constraints on thrust wedge development, northwest Himalaya, Pakistan. *Geological Society of America Special Papers, 232*, 113-128.

Butler, R. W., Coward, M. P., Harwood, G. M., & Knipe, R. J. (1987). Salt control on thrust geometry, structural style and gravitational collapse along the Himalayan mountain front in the Salt Range of northern Pakistan. *Dynamical geology of salt and related structures. Academic Press, London*, 339-418.

Calassou, S., Larroque, C., & Malavieille, J. (1993). Transfer zones of deformation in thrust wedges: An experimental study. *Tectonophysics, 221*(3), 325-344.

Chapple, W. M. (1978). Mechanics of thin-skinned fold-and-thrust belts. *Geological Society of America Bulletin, 89*(8), 1189-1198.

Costa, E., & Vendeville, B. C. (2002). Experimental insights on the geometry and kinematics of fold-and-thrust belts above weak, viscous evaporitic décollement. *Journal of Structural Geology, 24*(11), 1729-1739.

Cotton, J. T., & Koyi, H. A. (2000). Modeling of thrust fronts above ductile and frictional detachments: Application to structures in the Salt Range and Potwar Plateau, Pakistan. *Bulletin of the Geological Society of America, 112*(3), 351-363.

Dahlen, F. (1990). Critical taper model of fold-and-thrust belts and accretionary wedges. *Annual Review of Earth and Planetary Sciences, 18*, 55.

Dahlen, F. A., & Suppe, J. (1988). Mechanics, growth, and erosion of mountain belts. *Geological Society of America Special Papers, 218*, 161-178.

Dahlen, F. A., Suppe, J., & Davis, D. (1984). Mechanics of fold-and-thrust belts and accretionary wedges: Cohesive Coulomb Theory. *Journal of Geophysical Research, 89*(B12), 10087.

Davis, D., Suppe, J., & Dahlen, F. A. (1983). Mechanics of fold-and-thrust belts and accretionary wedges. *Journal of Geophysical Research, 88*(B2), 1153.

Davis, D. M., & Engelder, T. (1985). The role of salt in fold-and-thrust belts. *Tectonophysics, 119*(1–4), 67-88.

Davis, D. M., & Engelder, T. (1987). Thin-skinned deformation over salt. *Dynamical geology of salt and related structures*, 301-337.

Gretener, P. (1981). Pore pressure, discontinuities, isostasy and overthrusts. *Geological Society, London, Special Publications, 9*(1), 33-39.

Gutscher, M.-A., Kukowski, N., Malavieille, J., & Lallemand, S. (1996). Cyclical behavior of thrust wedges: Insights from high basal friction sandbox experiments. *Geology, 24*(2), 135-138.

Jia, C. (1997). The features of structure and petroleum geology on tarim basin of China: Beijing, Petroleum Industry Press.

Koyi, H. A., Hessami, K., & Teixell, A. (2000). Epicenter distribution and magnitude of earthquakes in fold-thrust belts: Insights from Sandbox Models. *Geophysical Research Letters, 27*(2), 273-276.

Letouzey, J., Colletta, B., Vially, R., & Chermette, J. (1995). Evolution of salt-related structures in compressional settings. *AAPG Memoir, 65*, 41-60.

Li, S., Wang, X., & Suppe, J. (2012). Compressional salt tectonics and synkinematic strata of the western Kuqa foreland basin, southern Tian Shan, China. *Basin Research, 24*(4), 475-497.

Lohrmann, J., Kukowski, N., Adam, J., & Oncken, O. (2003). The impact of analogue material properties on the geometry, kinematics, and dynamics of convergent sand wedges. *Journal of Structural Geology, 25*(10), 1691-1711.

Luján, M., Storti, F., Rossetti, F., & Crespo-Blanc, A. (2006). Extrusion vs. accretion at the frictional-viscous décollement transition in experimental thrust wedges: the role of convergence velocity. *Terra Nova, 18*(4), 241-247.

Mandal, N., Chattopadhyay, A., & Bose, S. (1997). Imbricate thrust spacing: experimental and theoretical analyses *Evolution of geological structures in micro-to macro-scales* (pp. 143-165): Springer.

Mitra, S. (2003). A unified kinematic model for the evolution of detachment folds. *Journal of Structural Geology, 25*(10), 1659-1673.

Mulugeta, G. (1988). Modelling the geometry of Coulomb thrust wedges. *Journal of Structural Geology, 10*(8), 847-859.

Mulugeta, G., & Koyi, H. (1992). Episodic accretion and strain partitioning in a model sand wedge. *Tectonophysics, 202*(2), 319-333.

Oldham, R. (1921). Know your faults. *Quart. J. Geol. Soc, 77*.

Smit, J. H. W. (2003). Deformation of brittle-ductile thrust wedges in experiments and nature. *Journal of Geophysical Research, 108*(B10).

Vidal-Royo, O., Koyi, H. A., & Muñoz, J. A. (2009). Formation of orogen-perpendicular thrusts due to mechanical contrasts in the basal décollement in the Central External Sierras (Southern Pyrenees, Spain). *Journal of Structural Geology, 31*(5), 523-539.